University of Groningen

Master Research Project

Exfoliation of $PtBi_2$, $Pt(BiTe)_2$, and $PtTe_2$ on Ag(111)/mica in UHV, Alongside Chamber Optimization

Author
Jouke de Boer

Supervisor & First Examiner
Dr. Antonija Grubišić-Čabo

Second Examiner
Prof. Dr. Marcos H. D. Guimarães

April 4, 2026

ABSTRACT

This research aims to address the challenge of reliably producing large, high-quality monolayer crystals of topological materials, as traditional exfoliation methods are limited by low yield, contamination, and poor substrate adhesion. In pursuit of this objective, the effectiveness of ultra-high vacuum (UHV) kinetic *in situ* single-layer synthesis (KISS) exfoliation of $PtBi_2$, $Pt(BiTe)_2$, and $PtTe_2$ on annealed and sputtered Ag(111)/mica was evaluated. The characteristic properties of the exfoliated crystals were analyzed using optical microscopy, atomic force microscopy (AFM), low-energy electron diffraction (LEED), and X-ray photoelectron spectroscopy (XPS). Via optical microscopy, the surface area of the exfoliated $PtBi_2$ crystals was determined to be the largest, whereas the $PtTe_2$ flakes exhibited the smallest surface area. AFM measurements confirmed that the crystal thicknesses are consistent with monolayer values. Furthermore, LEED analysis verified the presence of an exfoliated $Pt(BiTe)_2$ flake, with its domain rotated $26.06 \pm 0.08°$ with respect to the Ag(111)/mica. Lastly, XPS detected the Pt 4f peak at each analyzed exfoliation site, the Bi 4f peak was measured at the exfoliation sites of $PtBi_2$ and $Pt(BiTe)_2$, and the Te 3d signal was identified at the exfoliation sites of $Pt(BiTe)_2$ and $PtTe_2$. The experimental peak positions and spin-orbit splittings are consistent with values reported in literature, with the exception of the Pt 4f peak of samples containing bismuth and the Te 3d peak of $Pt(BiTe)_2$. Building on the experience and insight gathered during the KISS exfoliation process, an UHV KISS exfoliation chamber was designed using FreeCAD to visualize and discuss design changes aimed to improve exfoliation efficacy, efficiency, visibility, and reproducibility. Collectively, the findings of this research establish UHV KISS exfoliation as a promising approach for the production of large-area mono- and multilayer $PtBi_2$, $Pt(BiTe)_2$, and $PtTe_2$ crystals on Ag(111)/mica substrates.

Contents

1 Introduction **1**

2 Theory **2**
- 2.1 Topological Materials . . . 2
  - 2.1.1 Dirac and Weyl Semimetals . . . 2
  - 2.1.2 Topological Insulators . . . 3
- 2.2 The Electronic Properties of Layered Metals . . . 3
- 2.3 Applications of 2D Topological Insulators . . . 4
  - 2.3.1 Spintronic devices using topological insulators . . . 4
  - 2.3.2 Magnetoelectronic devices using topological insulators . . . 5
- 2.4 Kinetic *In Situ* Single-layer Synthesis . . . 6
- 2.5 Vacuum Systems . . . 7
  - 2.5.1 Pumps of the vacuum system . . . 8
  - 2.5.2 Vacuum Gauges . . . 9
  - 2.5.3 General vacuum system requirements . . . 9

3 Methodology **10**
- 3.1 Low-Energy Electron Diffraction . . . 10
  - 3.1.1 LEED Instrumentation . . . 11
  - 3.1.2 The Characteristic LEED Diffraction Pattern . . . 12
- 3.2 Optical Microscopy . . . 14
  - 3.2.1 The functioning of a compound microscope . . . 14
- 3.3 X-ray Photoelectron Spectroscopy . . . 15
  - 3.3.1 Sample Requirements and Applications of XPS . . . 15
  - 3.3.2 The Principle of XPS . . . 15
  - 3.3.3 XPS Instrumentation . . . 16
  - 3.3.4 Sample Characterization . . . 17
- 3.4 Atomic Force Microscopy . . . 18
  - 3.4.1 AFM Setup . . . 18
  - 3.4.2 AFM Modes . . . 19

4 Results **20**
- 4.1 Vacuum Chamber Design Optimization . . . 20
- 4.2 LEED Characterization . . . 22
- 4.3 Optical Microscope Results . . . 23
- 4.4 AFM Results . . . 25
- 4.5 XPS Results . . . 28

5 Discussion **33**
- 5.1 The Impact of Vacuum System Modifications . . . 33
- 5.2 Critical Assessment of the Exfoliation Result . . . 33

6 Conclusion **35**

References **35**

Appendices **40**
- A Technical Drawings of Vacuum System Components . . . 41
- B Additional Optical Microscope Images . . . 42
- C Supplementary High Resolution XPS Scans . . . 43
- D Atomic Percentages of Chemical Environments . . . 44

1 Introduction

The discovery of graphene in the early 2000s marked a breakthrough in materials science. It highlighted how reduced dimensionality can dramatically influence the electronic properties of materials, inspired research on two-dimensional (2D) materials aimed at enabling novel technological innovations, and was honored with the 2010 Nobel Prize in Physics.[1]

Distinctive electronic properties also appear in topological insulators (TIs), making them intriguing candidates for further research. In TIs, electrical conduction occurs along topologically protected edge/surface states, while the bulk remains insulating. The properties of TIs have been proven to be valuable in the field of spintronics and magnetoelectronics.[2, 3] In spintronic devices, TIs enable efficient manipulation of spin states via spin-orbit torque (SOT), offering low-energy control of magnetic layers. Furthermore, in magnetoelectronic systems they provide large anisotropic magnetoresistance (AMR) and planar Hall (PHE) effects at room temperature, enhancing the sensitivity of magnetic sensors.

The investigation of topological insulators in two dimensions is not only intriguing but also challenging, since not all materials can be produced as large high-quality 2D crystals. This makes characterizing their properties difficult or even impossible. Limitations in yield, substrate adhesion, and contamination in conventional exfoliation methods further emphasize the need for an improved method used to synthesize 2D materials.[4] A promising method aimed to solve these issues is called kinetic *in situ* single-layer synthesis (KISS).[5, 6] This method utilizes the difference in bond strength between the layers of a bulk crystal and its adhesion strength to a substrate. When the bulk crystal is brought into contact with the substrate, single-layer crystals can remain on the substrate's surface. The process is performed in ultra-high vacuum (UHV), with annealing and sputtering cycles used to clean the substrate and prevent contamination by adsorbates.

The aim of this research is to use the KISS to exfoliate $PtBi_2$, $Pt(BiTe)_2$, and $PtTe_2$ on Ag(111)/mica, to produce large high quality 2D crystals. Optical microscopy was used to analyze the size and shape of the crystals. Low-energy electron diffraction (LEED) provided information on the surface crystallinity and crystal orientation on the substrate. X-ray photoelectron spectroscopy (XPS) determined the chemical composition of the exfoliated crystals, while atomic force microscopy (AFM) measured their thickness and surface topography. Additionally, the UHV KISS vacuum system was designed using FreeCAD, enabling the visualization and discussion of potential modifications to its components aimed at improving the efficacy, efficiency, reproducibility, visibility of the exfoliation process.

Upon analysis of gathered results, an answer should be formulated to answer the research question: *How effective is KISS of $PtBi_2$, $Pt(BiTe)_2$, and $PtTe_2$ on Ag(111)/mica, and how can a vacuum chamber design be optimized to improve exfoliation efficacy, efficiency, reproducibility, visibility?*

2 Theory

The electronic structures of the van der Waals crystals investigated in this research are of significant interest to materials science as they exhibit unique topological properties. These materials can be classified as Dirac semimetals, Weyl semimetals, or topological insulators, depending on the metal and its dimensionality. The following subchapter will provide a brief description of the properties of each electronic structure, which will highlight their differences.

2.1 Topological Materials

Materials can be classified into the categories of conductor, semi-conductor and insulator, according to their electronic properties. In the field of condensed matter physics, topological materials have been identified as a new category. Unlike geometrical features such as shape or volume, the topological properties of a material are determined by topological invariants, which are integer quantities that remain unchanged under smooth deformations of the band structure.[7]

An example of an inherent topological invariant is the Chern number in quantum Hall systems, which counts the chiral edge states.[8] If this number is nonzero the material is inherently topologically nontrivial. In some materials, topological protection arises from a symmetry rather than being an inherent property of the material. One of these symmetries is time reversal symmetry, which ensures that the Hamiltonian remains unchanged when the direction of time is reversed. In the presence of time reversal symmetry, the bulk electronic structure can be characterized by a $\mathbb{Z}_2$ topological invariant. If the crystal structure has an inversion center, and band inversion alters the parity of the occupied energy bands then the material is $\mathbb{Z}_2$ invariant, and thus topological nontrivial.[9] Note that parity describes how a wavefunction behaves under spatial inversion. The wavefunction remains unchanged if parity is even, and changes sign under inversion if parity is odd.

Furthermore, materials with nontrivial topological band structures host new electronic states. Three-dimensional (3D) materials exhibit surface states, while 2D materials display edge states.[10] These states are topologically protected, remaining largely unaffected by perturbations and environmental influences.

2.1.1 Dirac and Weyl Semimetals

In Dirac semimetals two doubly degenerate bands cross in the Brillouin zone to form a fourfold degenerate Dirac point at the cross point, with linear dispersion in all three directions of the momentum space, as illustrated in Figure 1. Fourfold degeneracy implies that four energy states share the same energy at a single point in momentum space, two of these degenerate states arise from spin ($\pm\frac{1}{2}$), the other two arise from chirality (±1) chirality. These Dirac semimetals contain Dirac fermions that appear as quasi particles near the Dirac points in the semimetal, these are massless low-energy electronic excitations in the material.

When time-reversal or inversion symmetry is broken, the Dirac point splits into two nondegenerate Weyl points with opposite chirality, giving rise to Weyl quasi particles whose energy bands form two separate Weyl cones. The surface projections of these Weyl points are connected by open lines in momentum space, which host topological surface states.[11]

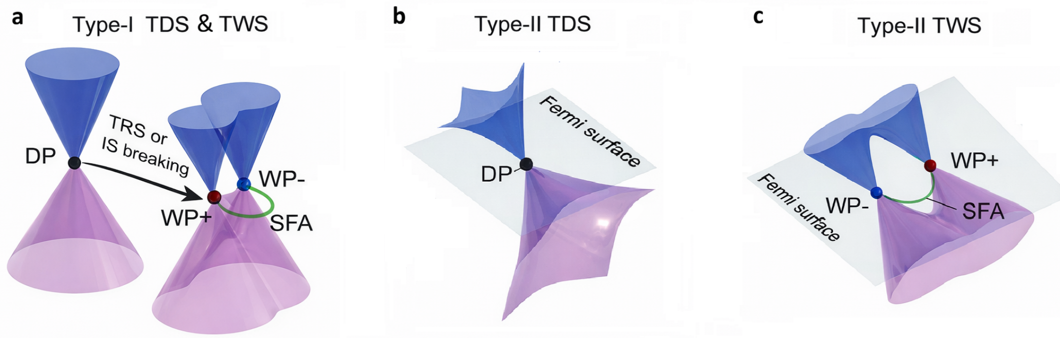

Figure 1: Electronic band structure schematic of topological Dirac semimetals (TDS) and topological Weyl semimetals (TWS). a) Dirac point (DP) splits into Weyl points with chirality (WP±) through time-reversal symmetry (TRS) or inversion symmetry (IS) breaking, producing a surface Fermi arc (SFA). b) Type-II TDS c) Type-II TWS. Image adapted from Reference [12].

Type-I semimetals are Lorentz invariant and have an isotropic electronic structure near the Dirac or Weyl points, leading to nearly uniform transport properties.[12] In contrast, type-II Dirac and Weyl semimetals break Lorentz invariance due to strongly tilted Dirac or Weyl cones. This leads to direction dependent velocities and electron hole pockets, resulting in anisotropic transport phenomena, such as directional-dependent conductivity. For Weyl nodes specifically, each node still carries a chirality ± 1, thus the breaking of Lorentz invariance can even produce anisotropic chiral electron transport.[13]

2.1.2 Topological Insulators

A topological insulator (TI) is a material with an insulating bulk and electronically conducting edge states in two dimensional materials, or surface states in three dimensional materials.[14] The bulk of the material is insulating due to a band gap in its electronic structure, while the conducting edge or surface states result from its non-trivial topology. Inherent topological protection arises purely from bulk topology, while symmetry protected topological protection depend on both topology and a specific symmetry, resulting in electronic states with stronger or weaker topological protection.[15]

2.2 The Electronic Properties of Layered Metals

Bulk $PtTe_2$ forms a P31m crystal and is a Type-II Dirac semimetal, the counterpart of $PtTe_2$ is $PtBi_2$ and has several crystal structure types.[16, 17] This research will focus on and use the trigonal structure with space group P31m, the bulk variant of this crystal has type-I Weyl structure.[18, 19] It can be beneficial to dope $PtTe_2$ using bismuth, altering its original electronic structure: More specifically, it would raise its Dirac to the Fermi level, creating an electronic structure with better electron conduction while keeping specific electronic properties that are inherent to the Type-II semimetal.

When reducing the dimensionality of these materials to 2D, the electronic structure changes with it. There is research to suggest $PtTe_2$ becomes a metal in 2D,[16] although there is other convincing experimental evidence to suggest that single layer $PtTe_2$ is a semiconductor with a band gap of +0.79 eV.[20] Furthermore, 2D T-$PtBi_2$ is a topological insulator which possesses multiple topological gaps, each gap protects an edge state.[21] Doping $PtBi_2$ with tellurium to create $Pt(BiTe)_2$ lowers the energy of the topological

edge states closer to the Fermi level, increasing electron conduction while preserving the topological character of $PtBi_2$.

2.3 Applications of 2D Topological Insulators

Topological insulators possess an electronic band structure that offers opportunities that could lead to revolutionary electronic developments, these developments lie in a variety of fields, such as topological spintronics and magnetoelectronics.[2, 3] This subchapter will provide a brief overview of the applications of topological insulators in spintronics and magnetoelectronics.

The applications discussed in this subchapter are based on the use of 3D topological insulators, whereas the materials fabricated in the experiments are 2D TIs. It is important to note that many of the functionalities demonstrated in 3D topological insulators can also be realized in 2D materials, with the added advantage of improved scalability and easier integration into device architectures, indicating the importance of the production of these specific 2D materials.

2.3.1 Spintronic devices using topological insulators

In the field of spintronics the SOT is used to efficiently flip spin states within a magnet using low level electrical energy, this is achieved through the use of a heterostructure consisting of a heavy metal or a TI in combination with a magnetic material, typically a ferromagnet.[2] The SOT of heavy metal/ferromagnet heterostructures have been widely investigated, unfortunately further developments have been hindered by their low spin Hall angle $\theta_{SH} = \frac{J_s}{J_c}$, where J_s represents the spin current and J_c represents the charge current.[22] The spin Hall angle thus describes how efficiently a charge current is converted into a spin current.

The relatively large θ_{SH} of TIs has been attributed to TIs exhibit naturally strong spin-orbit coupling (SOC), SOC is the interaction between an electron's spin and its orbital motion in an electric field and gives rise to the spin Hall effect in bulk TIs.[23] This effect causes electrons with opposite spins to be deflected from each other, producing spin separation perpendicular to the applied current. In TIs, SOC gives rise to topological surface states, topological surface states are electronic states where each electron's spin is locked perpendicular to its momentum, this is a phenomenon called spin-momentum locking.[24]

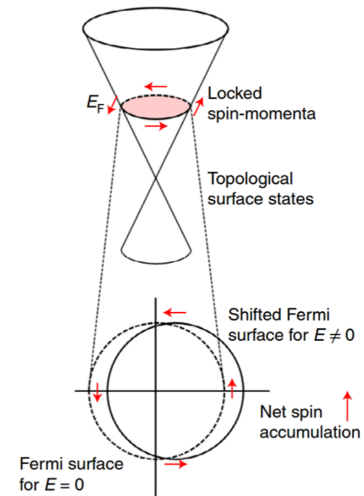

Figure 2: Spin-momentum locked surface states in a topological insulator (TI) shift the Fermi surface, generating transverse non-equilibrium surface spin accumulation. Image adapted from Reference [2].

When an in-plane charge current is applied, the Fermi circle of the topological surface state shifts in momentum space, as shown in Figure 2, this producing surface spin accumulation perpendicular to the in-plane current. Each point on the Fermi circle has a corresponding spin magnetic moment indicated by the red arrows, the shifting of the Fermi surface determines what spin will accumulate. This also implies that a pure spin current can be naturally obtained when passing a charge current through the TI.[25] The spin magnetic moments are opposite to the corresponding spin angular momenta, this spin angular momentum is

transferred to the adjacent magnetic layer through SOT. The resulting torque can act on a ferromagnetic or antiferromagnetic layer to flip its spin states, enabling low-energy electrical control of magnetic order.

In contrast, heavy metals do not exhibit spin-momentum locking resulting in less coherent spin currents, consequently their SOT is weaker compared to that of topological insulators.

2.3.2 Magnetoelectronic devices using topological insulators

From the previous discussion, it is clear that spintronics studies the electron's spin and how it can be used to store, manipulate, or transport information. The field of magnetoelectronics involves magnetoelectricity, which is the phenomenon where an electric polarization is induced by an applied magnetic field, or conversely, a magnetization is induced by an applied electric field.[2] While all magnetoelectronics devices are related to spin and magnetism, not all spintronics devices rely on magnetoelectric effects.

In the field of magnetoelectronics achieving room-temperature high anisotropic magnetoresistance ratios in 2D is highly desirable to create magnetic sensors, however the magnetoresistance ratios achieved in room temperature heterojunction-free thin films remain limited to only a few percent.[26] In contrast, an anisotropic magnetic ratio of -39 % was realized at room temperature in the topological insulator β-Ag_2Te when exposed to a magnetic field of 9 T.[27]

This result was achieved by using a current and an applied magnetic field which are both in-plane and oriented at angle φ with respect to each other. The current and magnetic field configuration described has an effect on the AMR and the PHE, which in turn modify the longitudinal (R_{xx}) and transverse (R_{xy}) resistances, respectively. AMR and PHE were originally observed in ferromagnetic systems arising from spin-related anisotropic scattering, recently these effects have also been reported in topological materials, such as Weyl/Dirac semimetals and topological insulators, causing phenomena like anisotropic back scattering from tilted Dirac cones.[3, 28]

The tilting of the Dirac cone modifies the spin textures, causing anisotropic electron scattering on the Fermi surface and directional the depended electrical resistance, this is schematically shown in Figure 3a.[29] The Fermi surface is depicted as a closed black ellipse in Figure 3b, the wavy line represents the phonon annihilation process caused by absorbing of an electron and is indicated with b_q, and the red and black arrows are spin and momentum directions of the Fermi surface states, respectively.

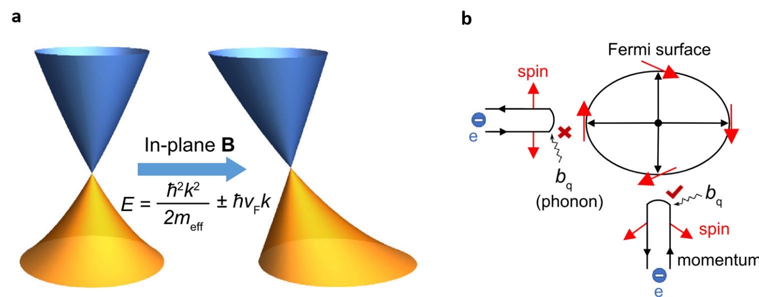

Figure 3: The process which regulates the planar Hall effect amplitudes in topological insulators. a) Schematic of the Dirac cone tilted by the magnetic field, and b) corresponding Fermi surface showing the modified spin texture. Image adapted from Reference [3].

Phonon absorption changes an electron's momentum to a new point on the Fermi surface, with scattering occurring only if the electron's spin aligns with the final state, the degree of this spin- and momentum-selective scattering can be increased by increasing the magnetic field strength. Consequently, increasing the field strength enhances the PHE, amplifying the AMR perpendicular to the current and producing a measurable transverse voltage drop, allowing for the detection of magnetic fields even at low supply voltages.

2.4 Kinetic *In Situ* Single-layer Synthesis

The importance of 2D materials is undeniable, but unfortunately creating these material has been proven to be rather challenging. After 2D materials were discovered in the early 2000s various techniques have been used to create them.[30] The first and simplest technique developed involves mechanically exfoliating materials with sticky tape.[31–33] The simplicity of the technique makes it an appealing method when studying these materials, although it does come with disadvantages. For example, the adhesive from the tape can remain on the sample, contaminating the surface with a polymeric residue.[34] This technique is also not suitable when exfoliating brittle crystals, since the likelihood of successful exfoliation is low. These limitations highlight the need to develop a new and improved exfoliation method, which needs to increase material yield, control substrate adhesion, manipulate lateral dimensions, and minimize contamination. This will produce higher quality 2D materials and expand the range of producible 2D materials.

The KISS method was developed in 2023 to address the limitations of conventional exfoliation techniques.[5] KISS consists of three main steps, which are shown in Figure 4. The first step consists of cleaving the bulk crystal inside the UHV environment, to expose a clean surface of the bulk crystal. The substrate is cleaned using sputtering and annealing cycles. Following this step, both surfaces are brought in contact. The forces holding the crystal layers together are weak van der Waals forces, which are weaker than the attractive forces between the crystal and the substrate. This difference in attraction allows for the removal of thin flakes from the crystal, which stay attached to the sample.

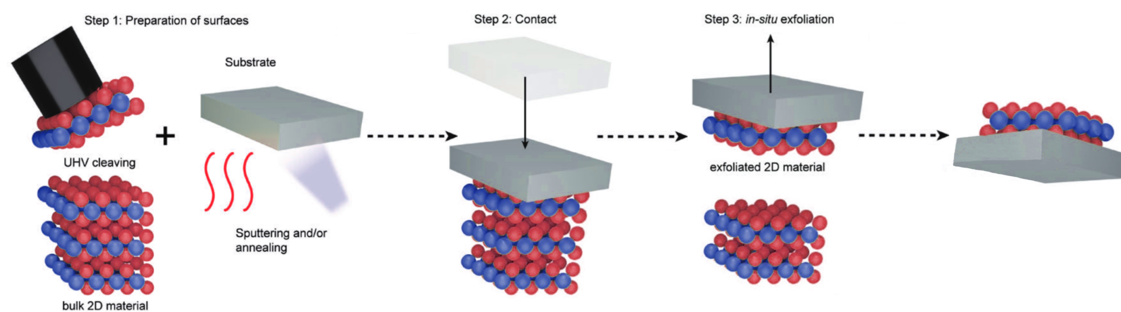

Figure 4: Schematic overview of the kinetic in situ single-layer synthesis exfoliation procedure. Image adapted from Reference [5].

KISS takes place in UHV to avoid surface contamination, significantly increasing the strength bond strength between the bulk crystal and substrate during exfoliation by reducing adhesion of adsorbates like oxygen, carbon, and nitrogen.

Furthermore, sputtering using positive argon ions reduces the amount of adsorbates on the substrate's surface even further. This is done by introducing a small amount of argon into the vacuum chamber until the pressure stabilizes at 3.2×10^{-6} mbar, an

acceleration voltage of 1.5 kV is then used for to accelerate the Ar^+ ions in the direction of the sample for a duration of 30 minutes. Ion bombardment introduces surface defects that can be resolved using thermal annealing the sample to promote surface diffusion, thus smoothening the surface.

Annealing is performed by resistively heating a filament close to the sample, the infrared radiation anneals the substrate to temperatures around 350°C. It is important to slowly heat the sample, because heating causes previously adsorbed species on the sample to desorb, increasing the chamber pressure. These released adsorbates can contaminate the vacuum environment and equipment within the chamber. The negative impact these released adhesives have can be mitigated by making sure the pressure within the chamber does not reach 4×10^{-8} mbar. Multiple sputtering and annealing cycles can be used to increase the surface cleanliness, thus increasing the effectiveness of KISS, with three cycles being the most common.

2.5 Vacuum Systems

Vacuum systems that are able to facilitate pressures in the range of 10^{-9} mbar are UHV systems, by definition.[35] This ensures a clean environment by lowering the amount of particles that can contaminate the sample's surface. From kinetic gas theory, the rate of molecules impinging on the surface and pressure in the chamber is given by

$$R = \frac{dN}{dt} = \frac{P}{\sqrt{2\pi M k_{\mathrm{B}} T}}, \tag{1}$$

where N is the number of molecules hitting the surface per unit time t, the pressure in the system is given by P, the molecular mass is described by M, Boltzmann constant is given by k_{B}, and T is the temperature in the chamber. The relation shown above indicates the importance of reaching a low pressure to reduce the contamination rate. Furthermore, the amount of gas being pumped out of the chamber by the system can be defined by the volumetric flow rate $Q = dV/dt$, with V being the volume of gas transferred the chamber per unit time t. This expression can can be rewritten using the ideal gas formula to obtain the relation shown below

$$Q = \frac{d(PV)}{dt} = k_{\mathrm{B}} T \frac{dN}{dt}, \tag{2}$$

Flow rate can describe various scenarios, such as the movement of gas through a tube connecting a vacuum system to a pump, the evacuation of particles from the vacuum system, or the influx of particles caused by a leak in the system's sealing. The process of evacuating the system can be described by

$$-\frac{dP}{dt} = P\frac{S}{V_c} - Q_0, \tag{3}$$

where S is the pumping speed, V_c describes the volume of the chamber, and Q_0 describes incoming flow of particles. When the incoming flow of particles is sufficiently small, Q_0 can be neglected. The relation above can be integrated to find the pressure in the system as a function of time given by

$$P(t) = P_0 e^{-\frac{S}{V_C}t}. \tag{4}$$

In conclusion, this relation shows that as pumping continues, the pressure in the vessel decreases more slowly over time. Reaching progressively lower pressures takes an exponentially increasing amount of time.

2.5.1 Pumps of the vacuum system

A typical vacuum system has a roughing pump, turbo pump and an ion pump, schematics of each pump is shown in Figure 5.

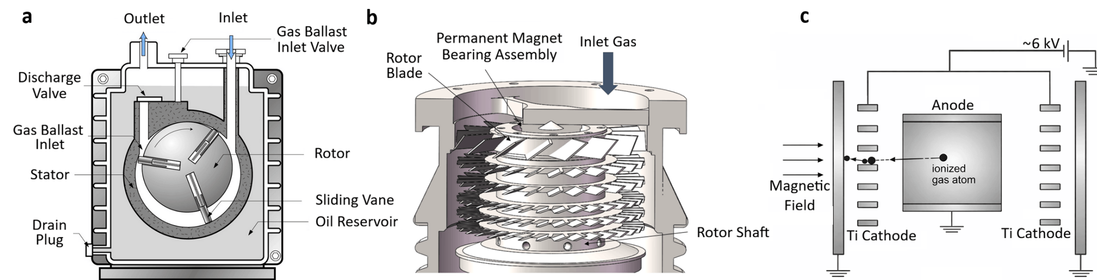

Figure 5: Schematic diagrams of various pumps used in ultra-high vacuum systems. a) Rotary vane pump, b) turbomolecular pump, and c) ion pump. Images adapted from References [35–37].

An oil-sealed rotary vane pump is a roughing pump capable of bringing a system down to roughly 10^{-3} mbar, this pressure is considered a prevacuum. A roughing pump works by trapping small packets of gas and pushing them toward the exhaust. The rotating vanes sweep the gas from the inlet side to the outlet side in a continuous cycle. Oil provides the sealing needed to prevent backflow and keep the gas moving in one direction.[36]

A turbomolecular pump can reduce the system pressure even further, operating in what is known as the molecular flow regime.[37] A turbomolecular pump has a large gas inlet in front of its main rotor, allowing a lot of gas to enter the pump. The momentum of the molecules of this gas is increased by collisions with the rotating blades that move at high-speeds. These can rotate up to 80,000 rpm, allowing for the turbomolecular pump to reach pressures as low as 10^{-10} mbar. Such pressures are only attainable if a roughing pump has first substantially lowered the vacuum chamber's pressure, otherwise molecular backflow would limit the minimum achievable pressure.[38]

When the pressure of the vacuum system is lowered significantly ion pumps are used to reduce the pressure even further.[35] Ion pumps operate across a pressure range between 10^{-3} mbar and 10^{-11} mbar, although use of this pump in higher pressure regimes can reduce the lifespan of the device. It functions by discharging a high voltage within the pump, creating a plasma. This discharge ionizes the residual gas molecules within the chamber, ionizing them by removing electrons from their electron shells. A magnetic field then confines these ionized particles and moves them through the pump towards the cathode, which is usually made out of titanium. Upon reaching the cathode the particles are absorbed or react chemically with the titanium. Furthermore, in some vacuum systems a titanium sublimation pump (TSP) is used alongside the ion pump. In a TSP, the voltage discharge sputters titanium atoms from a cathode, coating the pump's inner

surfaces. These titanium layers react chemically with residual gas molecules, enhancing the overall effectiveness of the vacuum. It is important to note that, unlike mechanical pumps, ion pumps do not remove gas from the system but instead convert it into forms that do not contribute to the measurable pressure.[39]

2.5.2 Vacuum Gauges

Similar to the pumps discussed previously, there is no single gauge that can effectively span the entire range between atmospheric pressure and UHV, which is why in two gauges are used, a Pirani gauge and an ion gauge. Schematics of both of these gauges are shown in Figure 6.

In the initial roughing stage, a Pirani gauge determines pressure by measuring how the gas's thermal conductivity affects the electrical resistance of a heated filament.[40] The filament is usually made out of platinum and is used in combination with a reference filament, which is maintained at ambient temperature and atmospheric pressure. They are wired in a Wheatstone bridge circuit, making it possible to compare the electrical resistances of the filaments. A current heats the filaments, and at higher pressures frequent collisions with surrounding gas molecules dissipate this heat. This lowers its resistance increasing the current through the filament in the chamber. While at lower pressures, fewer collisions with surrounding gas molecules occur, so the filament in the chamber retains more heat and its resistance remains higher. The lowest pressure regime this device can operate in is 10^{-5} mbar.

At lower pressures an ion gauge can take over and measure the gas pressure using a tungsten filament which emits electrons through thermic emission.[41] The filament is heated using the filament heating supply. The electrons generated are directed using the filament and grid bias supplies. The electrons are accelerated toward the gas, causing collisions that create positive ions. These ions are drawn to a central collector electrode, producing a current that corresponds to the gas pressure.

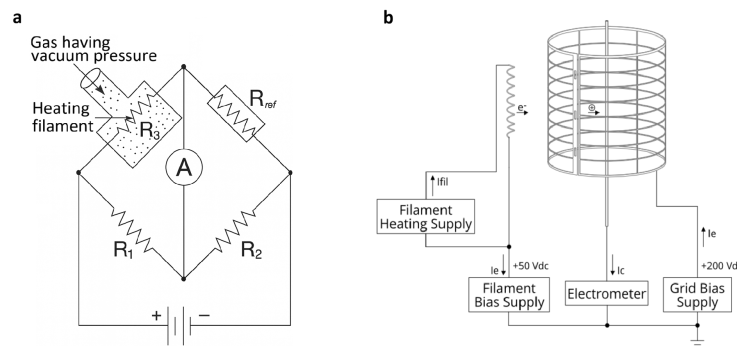

Figure 6: Vacuum system gauge schematics. a) Pirani gauge, b) ion gauge. Images adapted from References [40, 41].

2.5.3 General vacuum system requirements

Achieving and maintaining ultra-high vacuum requires materials that can endure extreme conditions. In particular, they need to withstand the high temperatures of a bake-out, a procedure where the vacuum system is heated above 100°C to remove adsorbed gases. Furthermore, the materials used must have low vapor pressure, be non-magnetic, and

maintain low gas permeability. Stainless steel is commonly used for chambers, and non-porous electrical insulators like ceramics are suitable for internal components. Plastics, rubber, and lubricants should be avoided due to outgassing.

Furthermore, the tubing connecting chambers should be short and straight to maximize conductance. Gaskets are used to seal the joints. Viton gasket are often used in high-vacuum applications for its reusability and cost-effectiveness. This material is limited to temperatures below 150 °C, and thus will degrade if the bake-out temperature used is too high. Hence, copper gaskets are used for UHV systems, this seal can withstand temperatures as high as 450°C these gaskets are, however, expensive and single-use.

3 Methodology

A new exfoliation chamber was designed using FreeCAD, using high contrast colors for clarity. The designs are based on constraints that define the structure's dimensions. Symmetry constraints are primarily used to ensure the design remains adjustable. This ensures that altering a single dimension does not affect the overall shape, all holes stay centered, all connections remain intact, and the structure retains its symmetry. Technical drawing of the design were also made using a workbench within the program called TechDraw, giving a detailed schematic of the designed vacuum chamber

The exfoliation method used is KISS,[5, 6] which produces thin crystal layers of $PtBi_2$, $Pt(BiTe)_2$, and $PtTe_2$ on Ag(111)/mica. In this method, Ag(111)/mica is kept in a vacuum chamber under UHV conditions, and undergoes cycles of sputtering and annealing. Sputtering is performed with positive argon ions, ionized by an emission current of 15 mA. The resulting ion beam is directed at the sample for 30 minutes. The substrate was subsequently annealed at a temperature of up to 350 °C. After three cycles of sputtering and annealing the crystal to be exfoliated is placed in the vacuum chamber, attached to the KISS holder. The top layer of this van der Waals metal crystal is then cleaved using sticky tape, after which it is pressed on the silver's surface for a short period of time, leaving behind a few layers of crystal. The exact theory behind this exfoliation technique is discussed was Subsection 2.4.

To analyze the success of the exfoliation attempt four surface characterization methods are used. Firstly, LEED is used to determine the diffraction pattern of the crystals present and the relative orientation of the crystals with respect to each other. This method is discussed in Subsection 3.1. Secondly, XPS is used to determine the chemical composition and chemical states of the sample material. This method is discussed in detail in Subsection 3.3. Furthermore, an optical microscope was used to determine the size, shape, and approximate thickness of the exfoliated van der Waals crystals. This technique is discussed in Subsection 3.2. Finally, a thickness measurement was performed using an AFM, this surface characterization technique is discussed in Subsection 3.4.

3.1 Low-Energy Electron Diffraction

Low-energy electron diffraction is a surface-sensitive technique used to probe the atomic structure of crystalline materials by analyzing the diffraction patterns of elastically scattered electrons. The electrons used have kinetic energies such that their de Broglie wavelengths are comparable to the lattice constants of most solids. The relation between

kinetic energy of the electron and wavelength is given by the function

$$\lambda = \frac{h}{\sqrt{2m_e E_{\text{kin}}}}, \tag{5}$$

where h is Planck's constant, m_e is the electron mass, and E_{kin} is the electron kinetic energy. The electron energies typically used range from $30 - 500$ eV, giving a de Broglie wavelength of approximately $0.5 - 2$ Å. Because this is comparable to lattice constants in crystal structures, LEED is highly sensitive to surface atomic structures.[35]

3.1.1 LEED Instrumentation

The LEED system generates a low-energy electron beam using a heated filament and directs it with a Wehnelt cylinder, a series of focusing lenses, and retarding grids. A schematic of this system is shown in Figure 7. The filament generates electrons through thermic emission, achieved by heated a tungsten wire by running a current through it.[42] LEED measurements are performed under a pressure of $P < 5 \times 10^{-8}$ mbar to minimize excessive filament degradation.

The emitted electrons are first shaped and their numbers limited by the Wehnelt cylinder. This is a negatively biased electrode with respect to the filament. The Wehnelt cylinder narrows the electron beam making it more collimated creating sharper diffraction spots, effectively acting like an electrostatic aperture. Increasing this negative bias reduces the number of electrons that escape, which lowers the beam intensity and can even completely stop the beam if made too negative.

Furthermore, the beam is guided by a set of electrostatic lens elements that focus the electrons onto the sample surface. Lens elements 1, 2, and 3 are controlled by a linear relationship between their voltage and the electron energy. They have a fixed offset which sets the base voltage, and a gain which determines how strongly the voltage changes linearly with energy. At low energies (< 50 eV), focus quality mainly depends on the offset, while at high energies (> 300 eV), the gain becomes more important. During this research, the setup was configured such that lenses 1 and 3 are on the same potential, and independent of lens 2.

Additionally, the suppressor connected to the retarding grids serve to reduce secondary and inelastically scattered electrons, which is achieved by applying a negative voltage. In order to make the electrons visible on the fluorescent screen it is necessary to apply a positive high voltage between 5 and 7 kV to the screen.

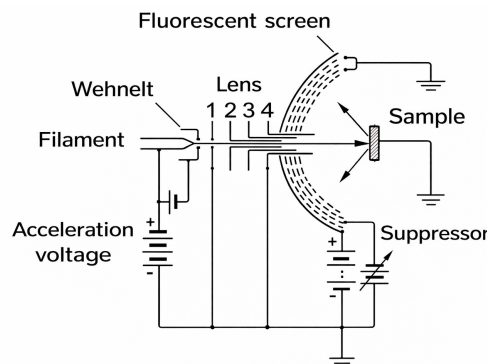

Figure 7: Schematic diagram of a four grid LEED system. Image adapted from Reference [42].

3.1.2 The Characteristic LEED Diffraction Pattern

The LEED diffraction pattern arises from elastically scattered electrons from the surfaces of the sample. Sharp, well-defined diffraction spots require the long-range periodicity of the surface, the diffraction pattern produced reflects the structure of the surface in reciprocal space. Moreover, it should be noted that the technique is non-kinematic, as electrons are expected to undergo multiple interactions with the surface and each other, resulting in multiple scattering events that alter spot intensities and produce additional diffraction spots.

Furthermore, the Ewald sphere is used to visualize the conditions in reciprocal space under which incident electrons are elastically scattered by surface to produce diffraction spots. The sphere's radius is equal to the magnitude of the incident wave vector, drawn in reciprocal space with its origin at the tip of the incident wave vector.

Discrete reciprocal lattice points are produced when a sample exhibits bulk periodicity and the probing depth is large, shown in Figure 8a, resulting in a limited number of diffraction spots since only the lattice points intersecting the Ewald sphere are observed. In contrast, when there is only surface periodicity the discrete reciprocal lattice points are elongated into continuous Bragg rods, shown in Figure 8b. The Ewald sphere can intersect these rods at multiple points, producing a larger number of visible diffraction spots.

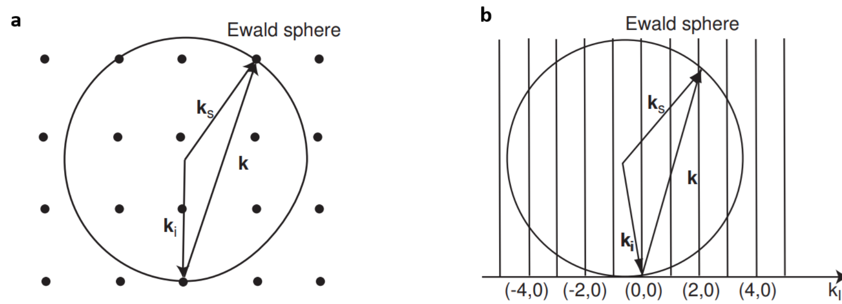

Figure 8: Ewald sphere construction for a) bulk crystals and b) surfaces and two-dimensional materials.[35]

The figure above essentially illustrates the Laue condition, which describes states that diffraction occurs when the difference between incident and scattered wave vectors equals a reciprocal lattice vector of the crystal. Mathematically this relation is given by the equation

$$(\mathbf{k}_\mathrm{s}^{||} - \mathbf{k}_\mathrm{i}^{||}) = \mathbf{\Delta k}^{||} = \mathbf{g}, \tag{6}$$

where $\mathbf{k}_\mathrm{s}^{||}$ and $\mathbf{k}_\mathrm{i}^{||}$ represent the wave vectors of the scattered and incident electrons parallel to the surface. The wave vector defines the direction of propagation and the momentum of the electron. $\mathbf{\Delta k}$ represents the difference in the incident and scattering wave vector due to the event. Finally, $\mathbf{g} = h\mathbf{b}_1 + k\mathbf{b}_2$ describes the reciprocal lattice vector, which corresponds to a specific set of lattice planes in the two-dimensional surface lattice. Note that h and k are Miller indices specifying the reciprocal lattice point, while $\mathbf{b}_1$ and $\mathbf{b}_2$ are the surface's reciprocal lattice vectors. The scattering process is elastic, thus $|\mathbf{k}_s| = |\mathbf{k}_i|$ needs to hold. Lastly, The Laue condition above disregards scattering

wave vectors perpendicular to the surface, because the surface lattice is assumed to be two-dimensional.

Not only does the energy of the electron determine if a scattering event takes place, it also effects the distance between diffraction spots on the fluorescent screen. This relationship is described by

$$d_{\mathrm{hk}} = R\sin(\Theta_{\mathrm{hk}}) = \frac{R}{|\mathbf{k}_{\mathrm{s}}|}|h\mathbf{b}_1 + k\mathbf{b}_2| = R\frac{\hbar}{\sqrt{2m_{\mathrm{e}}}}\frac{1}{\sqrt{E}}|h\mathbf{b}_1 + k\mathbf{b}_2|, \quad (7)$$

here d_{hk} is the distance on the fluorescent screen between the central beam and the diffraction spot indexed by (h, k). R radius of the screen. Θ_{hk} is the scattering angle associated with the (h, k) reflection. $\hbar$ is the reduced Planck constant, and m_e is the electron mass. Finally, E is the electron kinetic energy, increasing the energy decreases diffraction spot distances. A schematic of the sample's diffraction and the corresponding distance from the central beam is given by Figure 9.

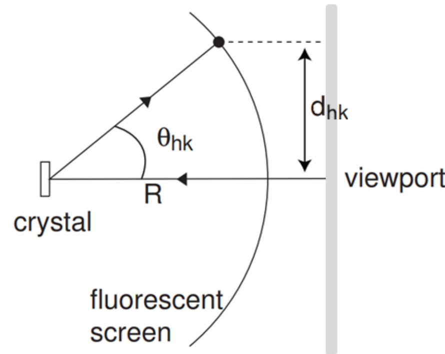

Figure 9: Schematic of electron diffraction from a sample onto a fluorescent screen. Image adapted from Reference [35].

The substrate used in this experiment is Ag(111)/mica. Silver has a face-centered cubic (FCC) crystal structure,[43] therefore the (111) plane gives rise to a hexagonal pattern in reciprocal space. Real and reciprocal space representations of this pattern are depicted in Figures 10a and 10b, respectively. $PtBi_2$, $Pt(BiTe)_2$, and $PtTe_2$ all have similar crystal structures, the top and side view of $PtTe_2$'s crystal structure is shown in Figures 10c and 10d. The hexagonal pattern observed in the top view leads to hexagonal symmetry in reciprocal space.

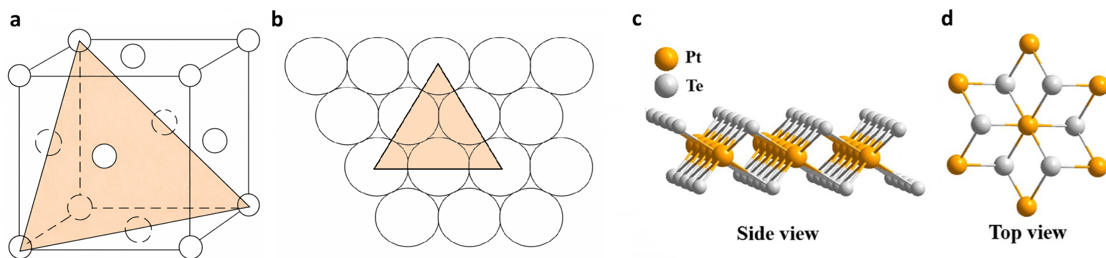

Figure 10: Schematic illustrations of a) real space face centered cubic (FCC) (111) crystal plane, b) reciprocal space FCC (111) crystal plane. c) Side view of $PtTe_2$, and d) top view of $PtTe_2$. Images adapted from References [44, 45].

The relative size of the hexagonal LEED pattern of silver compared to that of the exfoliated van der Waals crystals can be determined by using the equation

$$|\mathbf{b}_j| = \frac{2\pi\delta_{ij}}{|\mathbf{a}_i|\cos\alpha}, \tag{8}$$

where $\mathbf{b}_j$ is the j-th reciprocal lattice vector, δ_{ij} is the Kronecker delta, $\mathbf{a}_i$ is the i-th real-space lattice vector, and α is the angle between $\mathbf{b}_j$ and $\mathbf{a}_i$. Note that $\mathbf{a}_1 \perp \mathbf{b}_2$, and $\mathbf{b}_2 \perp \mathbf{a}_1$.

The lattice parameter of silver is $a = 4.08\,\text{Å}$.[46] The nearest-neighbor distance on the Ag(111) plane is therefore $[(\frac{1}{2}a)^2 + (\frac{1}{2}a)^2]^{\frac{1}{2}} = 2.88\,\text{Å}$. This length is equivalent to the value of $|\mathbf{a}_i|$. Given that $\alpha = 30°$, the corresponding reciprocal lattice vector has a magnitude can be determined to be $|\mathbf{b}_j| = 2.51\,\text{Å}$. Furthermore, the top view of the $PtTe_2$ crystal structure is hexagonal, thus the lattice parameter is equal to the magnitude of the real-space lattice vector, $a = |\mathbf{a}_i| = 4.00\,\text{Å}$.[47] The angle between $\mathbf{b}_j$ and $\mathbf{a}_i$ is again $\alpha = 30°$. Thus, in the case of $PtTe_2$ $|\mathbf{b}_j| = 1.81\,\text{Å}$.

The ratio both reciprocal lattice vector magnitudes is $\frac{2.51}{1.81} = 1.39$, indicating that the distance between reciprocal lattice spots of silver is around 39% larger than that of the metal that will be exfoliated.

3.2 Optical Microscopy

Optical microscopes offer a noninvasive way to determine the form, shape, size, and location of exfoliated crystal layers on the substrate. The information gathered using this technique is limited, however it does give of insight into the overall quality and suitability of the flakes for further experimentation. Furthermore, the results of the optical microscope shows differences in color and contrast. This makes it possible to quickly distinguish thinner regions from thicker ones, identify clean and uniform areas, and detect defects such as folds, tears, or contamination.

3.2.1 The functioning of a compound microscope

A compound microscope uses multiple lenses to magnify a specimen, this is illustrated in Figure 11. First light from a light source below the sample passes through the condenser lens, which focuses it through the specimen. Afterwards, the light passes through the objective lens above the specimen, forming a real inverted and magnified intermediate image. This intermediate image is then further magnified by the ocular eyepiece lens, producing a final enlarged virtual image the eye can see. Using this series of lenses these types of microscopes can resolve details down to approximately 0.2 µm.[48]

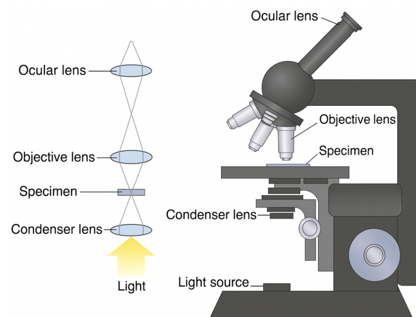

Figure 11: Diagram of a compound microscope, showing the path of light through the condenser, specimen, objective, and ocular lens to form a magnified image. Image adapted from Reference [48].

3.3 X-ray Photoelectron Spectroscopy

X-ray photoelectron spectroscopy is a quantitative surface-sensitive spectroscopic method that is able to measure the topmost 5 - 10 nm of any surface.[49] The technique irradiates the surface with a monochromatic X-ray beam to obtain the electron population spectra, making the technique part of the photoemission spectroscopy family. This emission allows the kinetic energy of the electrons to be measured, from which their binding energies can be determined. The results of XPS show a plot of intensity versus binding energy of the photo emitted core-level electrons, with the features of this plot being located at fixed binding energies. The locations of these features are material dependent, because each element has its own characteristic set of core-level binding energies.[50]

3.3.1 Sample Requirements and Applications of XPS

To allow XPS to measure a sample it needs have certain characteristic properties. First and most importantly, the material analyzed needs to be solid. Secondly, it needs to survive the X-rays used while analyzing its surface. Additionally, the technique requires high or ultra-high vacuum conditions, meaning the sample must remain stable without degradation or outgassing up to pressures of approximately 10^{-7} mbar for high vacuum and 10^{-11} mbar for ultra-high vacuum. Thankfully, many materials fit these criteria, including (in)organic compounds, semiconductors, metals, metal alloys, insulators.

This technique is used to determine the chemical composition of materials by evaluating the spectrum of photoemitted electrons across different binding energies. The positions of the peaks in this spectrum enable identification of the elements present, while their intensities determine the abundance of each element, allowing for semi-quantitative analysis of the surface composition. In addition, shifts in binding energy provide information on the chemical state of the elements, such as differences in oxidation state or bonding environment, which are related to the nature and strength of their chemical bonds. As a result, XPS provides detailed insight into both the elemental composition and the chemical environment at the surface, making it a valuable tool for studying surface-related processes.

3.3.2 The Principle of XPS

XPS is an application of the photoelectric effect, described by Einstein in 1905 and was awarded the Nobel Prize in 1921.[51]. In this technique electrons are emitted from the atoms in response to electromagnetic radiation. Einstein predicted that electrons would be ejected from a material if the energy of the incoming photons surpasses the electrons' binding energy.

When a material is irradiated, electrons are ejected from specific atomic orbitals, each characterized by a distinct binding energy. The number of electrons ejected from a core-level determines the intensity observed at that binding energy in the XPS spectrum. The binding energies of the core-level can be determined by measuring the kinetic energy of the emitted electrons, since the other factors impacting the electron's kinetic energy are known. The binding energy is calculated using the relation

$$E_K = E_{Photon} - E_B - \varphi, \tag{9}$$

here E_K is the kinetic energy of the photoelectron measured by the spectrometer. E_{Photon} is the energy of photon used to irradiate the sample, which is a known and

constant value. E_B is the binding energy of the core-level electron that is ejected. Lastly, φ is the work function of the material, defined by the difference between the vacuum energy level and the Fermi level of the solid.

The described ejection of the electron from its core shell is schematically shown in the form of an energy diagram in Figure 12.

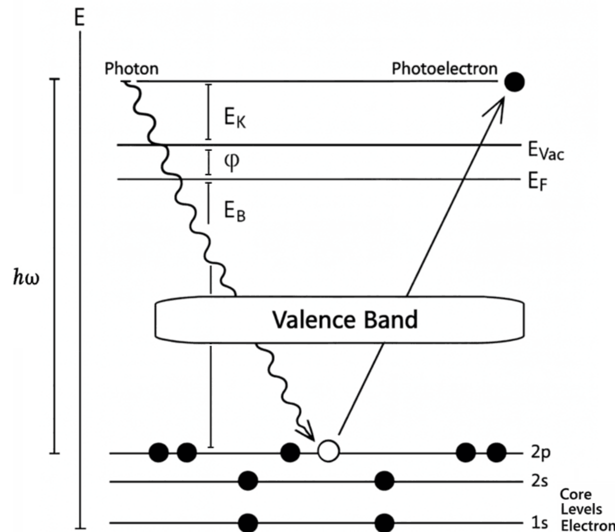

Figure 12: Schematic energy diagram of X-ray photoelectron spectroscopy (XPS), showing X-ray excitation of core electron. Here, E_K is the kinetic energy of the emitted electron, φ is the work function of the material, E_B is its binding energy, E_{Vac} is the vacuum level, E_F is the Fermi level, and $\hbar\omega$ is the photon energy. Image adapted from Reference [52].

3.3.3 XPS Instrumentation

In XPS, X-rays are typically generated by directing a high-energy electron beam ($\sim$ 15 keV) onto a metal anode, typically made from magnesium or aluminum. This produces characteristic κ_α emissions such as κ_α at 1250 eV for magnesium, and κ_α at 1490 eV for aluminum, with a linewidth of approximately 1 eV.[53] Aluminum filters are often used to minimize Bremsstrahlung background and satellite lines in the spectrum. Conventional lab sources produce spot sizes on the order of mm^2, whereas synchrotron sources provide tunable photon energies and smaller spot sizes, enabling more surface-sensitive measurements.

Before reaching the sample, the X-rays generated pass through a monochromator. This device uses Bragg reflections to suppress and filter out electromagnetic waves with unwanted wavelengths, only allows X-rays with a narrow energy range are able to reach the sample.[54] This increases spectral resolution, making it possible to distinguish smaller differences in energy between two features in the spectrum. While this device does increase spectral resolution and even reduces the X-ray's spot size, it also lowers the count rate which decreases the signal-to-noise ratio.

A hemispherical analyzer is used to measure the kinetic energy of the emitted photoelectrons. It consists of two hemispherical electrodes separated by a small gap, across which a voltage is applied to create a radial electric field. Electrons entering the analyzer

are bent along circular trajectories determined by their kinetic energy, and only those with the selected energy pass through the exit slit to the detector. To determine the kinetic energy of the electrons a position-sensitive multichannel detection plate can be used at the end of the analyzer.[55] Electrons of differing kinetic energies are focused on different positions along the plate, making it possible to distinguish between electrons of differing kinetic energies. Lastly, the analyzer's energy resolution depends on the pass energy and slit width, with lower pass energies yielding higher resolution at the cost of reduced count rates, again lowering the signal-to-noise ratio.

The complete XPS setup is schematically shown in Figure 13, illustrating the arrangement of the previously discussed components and their relative positions, which together enables the surface characterization of the sample.

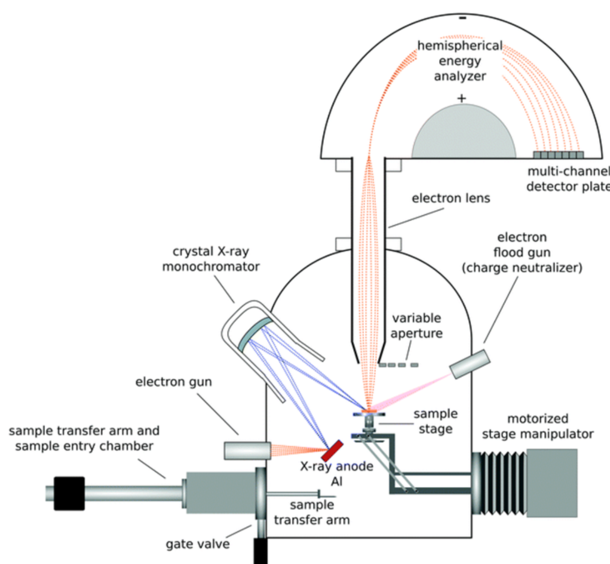

Figure 13: Schematic of an XPS setup. The electron gun generates X-rays on an aluminum anode, which are filtered and directed at the sample. The emitted electrons are detected by the multi-channel plate at the end of a hemispherical analyzer.[55]

3.3.4 Sample Characterization

Spin-orbit coupling arises from the interaction between an electron's orbital angular momentum (l) and its intrinsic spin (s), leading to a total angular momentum $j = l \pm s$. This interaction is strongest in heavier elements and causes core-level energy states to split into two distinct levels with different energies. Each split state has a degeneracy of 2j+1, which determines the relative intensity of the two peaks. In XPS, this splitting appears as a characteristic spin-orbit doublet, whose peak-area ratio is determined by the degeneracies of the two j states.

As an example, the substrate material used is Ag(111)/mica and its XPS spectrum consequently exhibits the spin-orbit split Ag 3d core-levels, as shown in Figure 14. For d orbital $l = 2$ and $s = \frac{1}{2}$, giving $j = 2 \pm \frac{1}{2}$. This yields $j = \frac{5}{2}, \frac{3}{2}$. These correspond to the Ag $3d_{5/2}$ and Ag $3d_{3/2}$ peaks observed in the XPS spectrum. Their degeneracies are $2j + 1 = 6, 4$, respectively. Producing an intensity ratio of 3:2. Furthermore, according to the literature, for Ag(111) one can expect the $3d_{5/2}$ peak at approximately 368.1 eV and the $3d_{3/2}$ peak near 374.1 eV.[50]

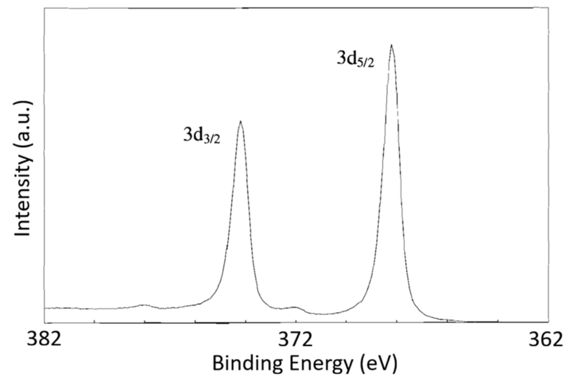

Figure 14: XPS spectra of the spin-orbit split Ag 3d core-level, showing Ag 3d$_{3/2}$ and Ag 3d$_{5/2}$ peaks. Image adapted from Reference [50].

These two peaks are not the only features expected in the XPS spectrum. The exfoliated metals platinum, tellurium, and bismuth have strong spin-orbit coupling in their core electrons, which leads to the additional spin-orbit split peaks in the XPS spectrum. In contrast, elements such as nitrogen and oxygen display a single spectral peak, as their 1s core-levels have $l = 0$, $s = 1/2$, and $j = 1/2$, resulting in no spin-orbit splitting.

3.4 Atomic Force Microscopy

The atomic force microscope is a scanning probe microscope with a resolution on the order of fractions of a nanometer, with measured forces in the range of 10^{-6}-10^{-10} N.[56] It can operate on samples that are conductors, semiconductors, and insulators, and is capable of functioning in air, vacuum, or liquid environments.[57]

3.4.1 AFM Setup

The AFM works by moving a sharp tip attached to a cantilever over the sample's surface. A laser beam is reflected off the cantilever onto a photodiode, where the position of the laser spot depends on deflection of the cantilever. The position of the sample is controlled using piezoelectric tubes, allowing imaging of surface topography, mechanical, electrical, magnetic, and chemical properties. A schematic of the standard AFM setup with the discussed components is shown in Figure 15.

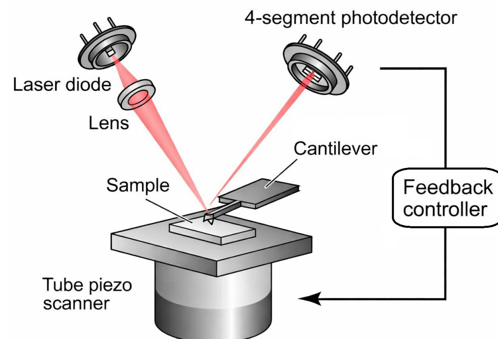

Figure 15: Schematic atomic force microscope (AFM) setup. Laser light is reflected off of the cantilever onto a photodiode, with its position depending on cantilever deflection. The sample's position is controlled via the piezoelectric tubes. Image adapted from Reference [58].

3.4.2 AFM Modes

The AFM can operate in various modes, examples of these are contact mode and dynamic mode. During contact mode the cantilever maintains a constant height while the deflection force is measured. This makes it possible to create a hight map of the surface. Alternatively, the force can be varied while keeping the height constant, producing a force map of the sample's surface.

Several dynamic modes exist. One of these is the tapping mode which is also called amplitude modulation (AM) mode, the operation of this setting is schematically depicted in Figure 16a. The other mode is the non-contact mode or frequency modulation (FM) mode, its operation illustrated in Figure 16b.

The AM mode, uses the amplitude of the cantilever amplitude as the feedback parameter. The z-position of the cantilever adjusted to maintain a set eigenfrequency.[59] In this mode, the cantilever remains close to the sample, periodically contacting it. The cantilever is typically driven using a gold-coated tip illuminated by a modulated blue laser, this is called blue drive, which causes the tip to thermally expand and contract. This allows precise control of the tip oscillation frequency, improving imaging stability and sensitivity.

Furthermore, the FM mode uses the change in cantilever frequency as its feedback parameter, and changes the cantilever tip hight to ensure the amplitude stays constant. In this mode, the frequency can be described by $f_0 = \frac{1}{2\pi}\sqrt{\frac{k}{m^*}}$, here k is the cantilever spring constant and m^* is its effective mass.

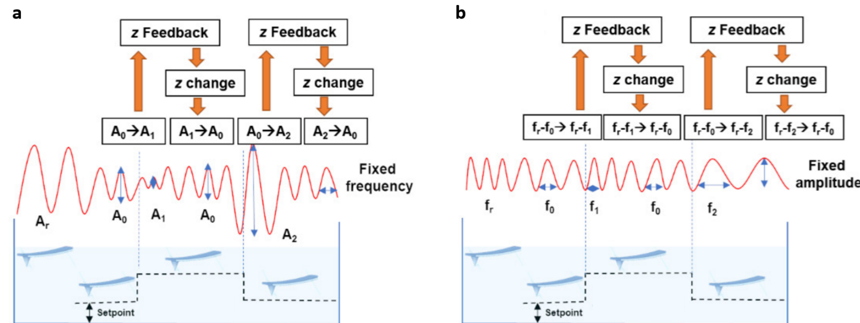

Figure 16: Schematic of dynamic AFM modes. a) Amplitude modulation (tapping) mode, b) frequency modulation (non-contact) mode. Images adapted from Reference [59].

To investigate the exfoliated crystal thickness the dynamic tapping mode of the AFM was used. Although AFM measurements of monolayer $PtBi_2$, $Pt(BiTe)_2$, and $PtTe_2$ on Ag(111)/mica substrates are not reported in the literature, related measurements provide useful reference values. The single-layer step height of $PtBi_2$ has been reported to be 6.0 Å, while a single layer of $PtTe_2$ within a series of stacked 2D layers was measured to be 5.22 Å.[21, 60] Providing an indication of the expected monolayer crystal height.

4 Results

4.1 Vacuum Chamber Design Optimization

The UHV KISS chamber was modeled using FreeCAD to visualize and analyze the current vacuum chamber design. The resulting design is shown in Figure 17, with key elements magnified for clarity. The chamber is rendered using a steel color scheme, reflecting the material from which the vacuum chamber is constructed. Components relevant to the exfoliation procedure are labeled, although gauges and pumps are omitted from the design to avoid unnecessary complexity. The bottom and back ports of the preparation and load lock chambers are not utilized during the exfoliation process, and are therefore closed with metal plates in the vacuum chamber model.

Technical drawings of key vacuum system components are available in Appendix A. These include the technical drawings of the preparation and load lock chamber, depicted in Figures 32a, and 32b, respectively. Furthermore, the sample holder features a wide and a thin side. The transfer arm is designed with a slot that grips the holder by its thin side, technical drawings of this arm are depicted in Figures 33a, 33b, and 33c. The transfer arm can move along, and rotate around, the x-axis. This allows the wider end of the sample holder to be inserted horizontally into a garage slot, or vertically into the sample slot at the base of the manipulator arm. The garage itself can move along the z-axis, with its technical drawings presented in Figures 34a, 34b, 34c, and 34d. The manipulator arm can move along the x-, y-, and z-axes and rotate around the z-axis, its technical drawings are shown in Figures 35a, 35b, 35c, and 35d.

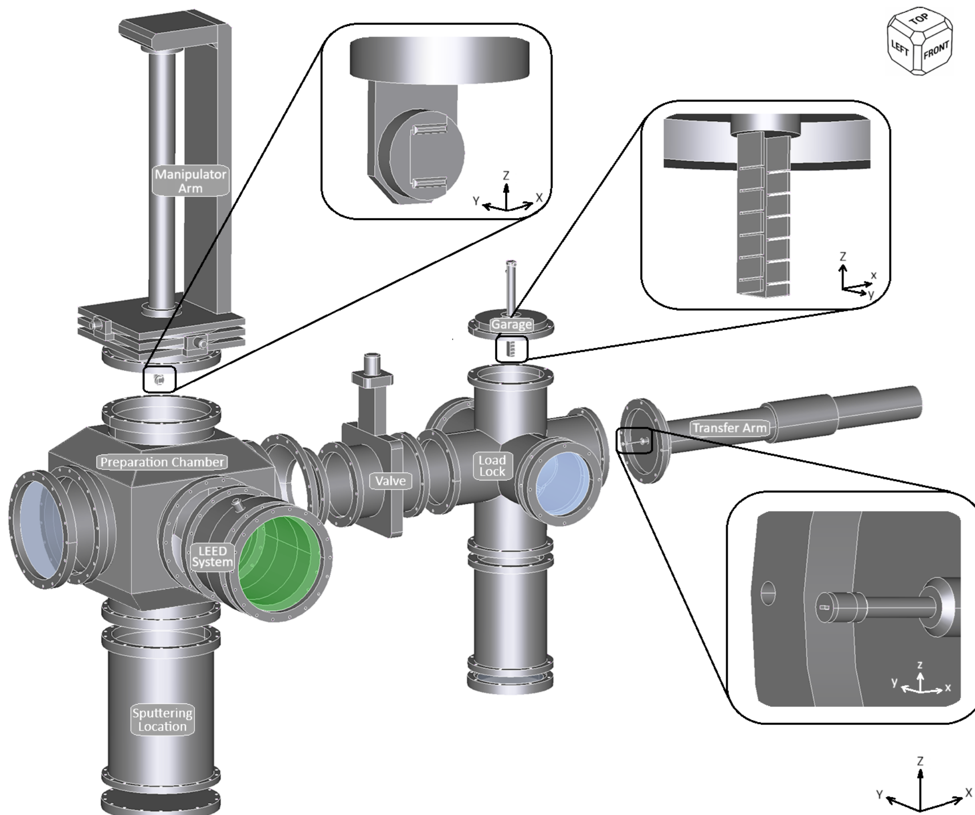

Figure 17: General overview of the designed vacuum system used for KISS, noteworthy elements are magnified.

To improve the design of the system, small changes can make a large difference in sample preparation time and consistency of exfoliation result. Currently, a heating element on the manipulator arm near the sample holder is used to anneal the sample to 350°C, several hours of cooling are required before the next sputtering cycle can begin. Adding a cooling element to the manipulator arm would reduce this cooling time. Substrate preparation involves multiple annealing and sputtering cycles, therefore reducing the time required for each cycle translates into a notable decrease in total processing time per substrate.

The manipulator arm currently accommodates only a single sample holder. Introducing slots below the existing holder would allow multiple substrates to be annealed at the same time, provided that corresponding heating elements are also incorporated. Similarly, by introducing additional sputtering guns that are directed at the sample holders, multiple substrates can be sputtered simultaneously.

Exfoliation consistency can be improved by minimizing variables that interfere with an optimal KISS process. After substrate cleaning in the preparation chamber, the transfer arm brings the bulk crystal into contact to exfoliate it. Rotation of the arm during this step reduces the effectiveness of KISS exfoliation and introduces variability between attempts. Restricting the arm to x-axis motion during exfoliation improves KISS effectiveness and enhances reproducibility.

Complimenting previous improvements, specific modifications to the current vacuum system can significantly enhance measurement capabilities and improve sample visibility during exfoliation. Currently, only LEED measurements are conducted within the KISS vacuum chamber. Requiring the sample to be exposed to ambient conditions before further analysis takes place, adversely affecting the results. To address this issue, the viewing gasket on the left side of the preparation chamber could be replaced by an additional vacuum chamber of similar size, which would be designated as a measuring chamber.

This measuring chamber would allow for the integration of multiple measurement systems, including XPS, AFM, and LEED. Optical microscopy could also be carried out through a viewing port, while the microscope itself remains outside the chamber. Enabling comprehensive characterization under ultra-high vacuum conditions. Additionally, relocating the LEED system to the measuring chamber would free space on the front of the preparation chamber for an additional viewing gasket, improving visibility of the sample during KISS. Additionally, since the rear of the preparation chamber is currently unused, a viewing gasket could be added to provide additional an additional observation angle to improve oversight of the exfoliation process.

In summary, the proposed vacuum system improvements show potential to enhance throughput and reproducibility by enabling simultaneous annealing, active cooling, and restricted transfer arm motion. Specific modifications, such as adding a dedicated measuring chamber and additional viewing gaskets, would complement these improvements by enabling *in situ* characterization under ultra-high vacuum conditions and improving sample visibility during exfoliation. However, challenges remain in achieving consistent bulk crystal positioning, multi-sample sputtering, and fully optimized transfer mechanics, which require further design refinements.

4.2 LEED Characterization

The three van der Waals crystals exfoliated under UHV conditions onto Ag(111)/mica were first examined using qualitative LEED. This surface characterization method requires a region of long-range order that is roughly 0.1 to 1.0 mm wide, corresponding to the width of the electron beam.[61] As a result, measuring small crystals on samples becomes more challenging.

The surfaces of the crystals exfoliated were also not uniform in thickness and structure, increasing the difficulty of this measurement even further. Despite considerable efforts to resolve LEED patterns for the $PtBi_2$ and $PtTe_2$ crystals, no diffraction signal was observed on the fluorescent screen. This suggests that the crystalline ordering of these materials on the substrate is relatively short or that the flakes are too small.

In contrast, the sample containing $Pt(BiTe)_2$ was successfully measured using LEED. The LEED measurements were performed using an incident energy of 125 eV, a Wehnelt bias of -43 eV, and a suppression voltage of 30 eV. To focus the electron beam, lenses 1 and 3 were set to 511 eV, while lens 2 was set to 15 eV. Before exfoliation of this metal took place LEED measurements were taken on the clean Ag(111)/mica substrate, which is depicted in Figure 18a. After exfoliation of $Pt(BiTe)_2$ on the substrate two new faint diffraction spots appeared on the fluorescent LEED screen, visible in Figure 18b. The brightness of the pattern depends on the crystal size and because the $Pt(BiTe)_2$ crystals on the substrate are relatively small, their spots appear dimmer than the silver spots. This same LEED result has been annotated for clarity, which is shown in Figure 18c, the red squares indicate the $Pt(BiTe)_2$ diffraction pattern and the blue squares indicate the silver diffraction pattern.

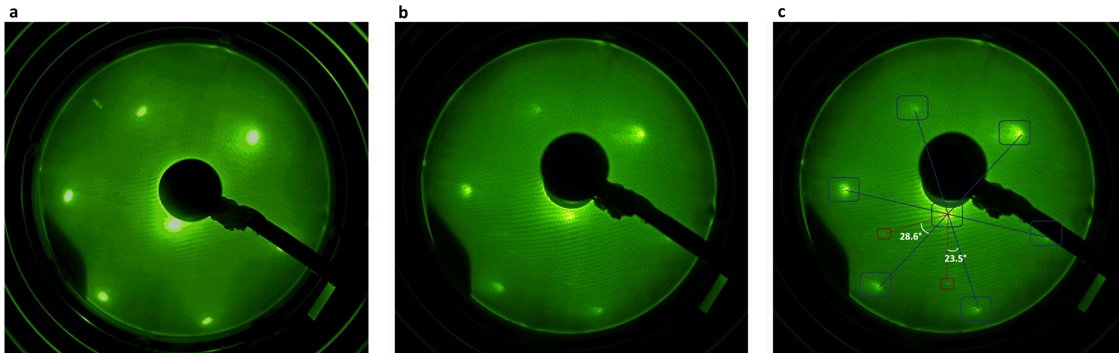

Figure 18: LEED characterization at 125 eV of a) Ag(111)/mica, b) exfoliated $Pt(BiTe)_2$ on Ag(111)/mica, and c) annotated $Pt(BiTe)_2$ (red) on Ag(111)/mica (blue).

The broadening of the Ag(111) diffraction pattern is attributed to a misalignment of the crystallographic orientation between silver domains in the substrate. Additionally, because the electron gun was not perpendicular to the sample surface, diffraction spots on one side of the fluorescent screen appear brighter and wider than on the other side.

The LEED patterns measured were hexagonal in nature, as expected and discussed in Subsection 3.1. The average distance between Ag(111) spots is 604 pixels and between $Pt(BiTe)_2$ spots 414 pixels, making silver's hexagonal pattern 45% larger, which exceeds the predicted value of 39% discussed in Subsection 3.1. The deviation of 6% from the theoretical prediction can be attributed to experimental factors, such as the sample's surface not being perfectly flat, and the direction of the electron gun not being exactly perpendicular to the surface of the sample.

Finally, the orientation of the LEED patterns relative to each other was measured in two different parts of the LEED pattern, this resulted in measurements of 28.6° and 23.5°, yielding an average $Pt(BiTe)_2$ crystal orientation on the substrate of $26.05 \pm 0.08°$.

4.3 Optical Microscope Results

Optical microscopy was used at varying magnifications to examine the three samples, potential regions containing single layer exfoliated metal crystals on the surface of the Ag(111)/mica substrate were identified, and measured in length, width, and area. The images shown have a color based on the filter used, which was optimized to show clear contrast between potential monolayer crystals and the silver's substrate. Given that annotations do obscure the substrate to monolayer transition slightly, unannotated images are provided in Appendix B for completeness. Furthermore, an increase in magnification results in less light entering the lenses, resulting in a darker image being displayed. making it more difficult to make out differences in material structure.

At a later stage of the research, specific regions were examined using an AFM to further probe the features of the exfoliated metal and to confirm crystal thickness, the areas selected for AFM analysis are indicated on the most magnified image of each crystal respectively.

A well-defined exfoliated multilayer $PtBi_2$ flake is observed on the Ag(111)/mica surface in Figure 19. Figure 19a shows the location of the crystal at 3.15× magnification, this image shows no significant surface contamination, with the region selected for further optical magnification is marked in white. Figure 19b provides a closer view at 12.6× magnification. In this image, a black "z"-shaped feature rotated by 90° is visible above the crystal, this is likely a scratch formed during the exfoliation process. Figure 19c shows the crystal at an increased magnification of 31.5×, showing multilayer $PtBi_2$ regions along with areas that may be monolayer. The crystal was measured to have a length of 211.45 ± 0.01µm, a width of 114.45 ± 0.01µm, and an area of 20028.12 ± 0.01µm^2.

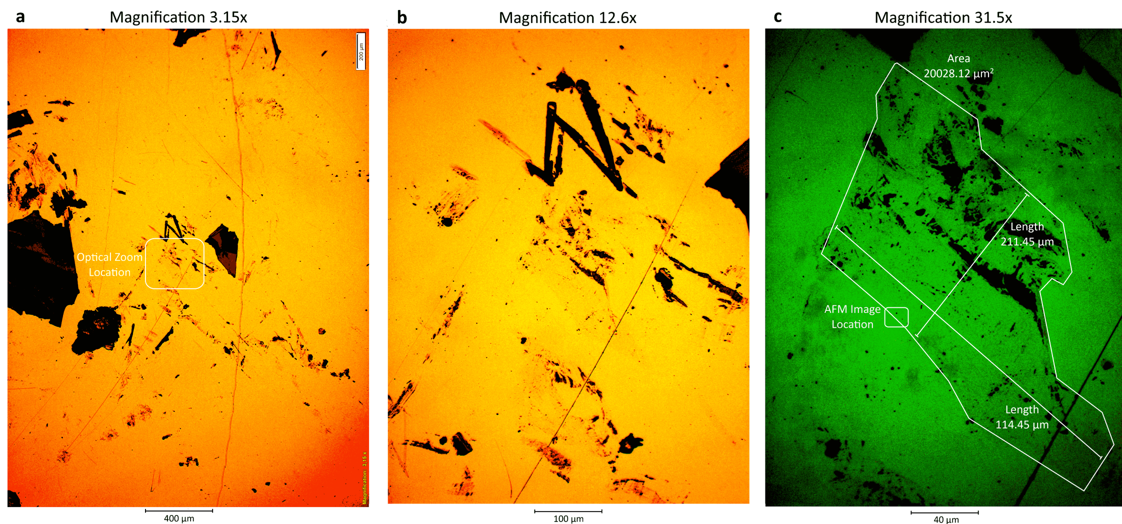

Figure 19: Optical microscope images of exfoliated $PtBi_2$ on Ag(111)/mica substrate at a) 3.15× magnification, b) 12.6× magnification, and c) 31.5× magnification with annotations indicating crystal length, width, and area.

$Pt(BiTe)_2$ was also successfully exfoliated and one of these exfoliation sites is presented in Figure 20a. This image was taken at a magnification of 3.15× and shows exfoliation was performed near the corner of the substrate, with no noticeable contamination present. Figure 20b provides a 12.6× magnified view of the flake revealing bulk, multilayer, and potential monolayer crystals. In Figure 20c, a 31.5× magnification image was used to measure the dimensions of the top crystal, yielding a length of 112.29 ± 0.01µm, a width of 47.47 ± 0.01µm, and an area of 2394.58 ± 0.01µm^2. Another potential monolayer crystal was found to have a length of 113.65 ± 0.01µm, a width of 20.65, ±0.01µm, and an area of 2129.68 ± 0.01µm^2, this crystal was subsequently examined in more detail using AFM.

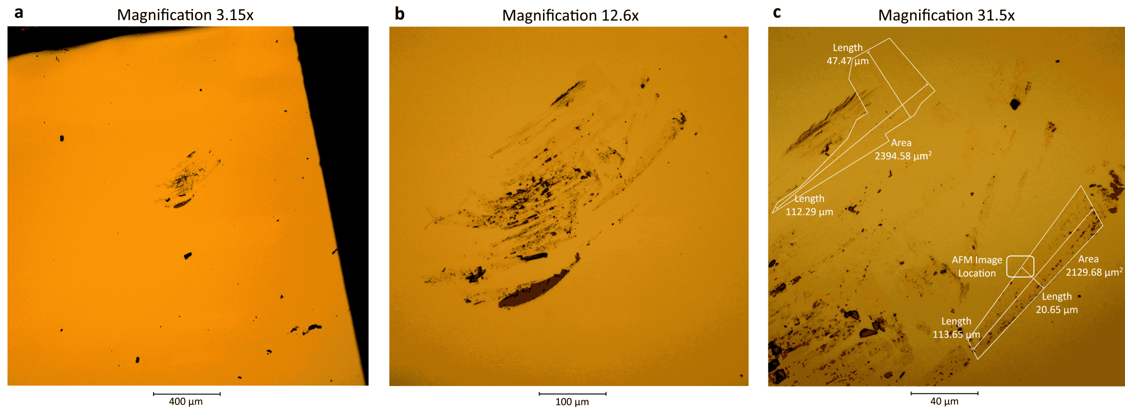

Figure 20: Optical microscope images of exfoliated $Pt(BiTe)_2$ on Ag(111)/mica substrate at a) 3.15× magnification, b) 12.6× magnification, and c) 31.5× magnification with annotations indicating crystal length, width, and area.

Lastly, the success of $PtTe_2$ exfoliation was limited, Figure 21a shows the outcome of one exfoliation attempt that features multilayer crystals near the bulk material. Above the exfoliation site, black horizontal scratches and holes are visible on the substrate surface, with no contamination is present. Figure 21b provides a further magnified view of the $PtTe_2$ flake, again showing a clean surface free of contamination. Finally, a magnification of 63× was used to determine the size of the crystal, which is shown in Figure 21c. The crystal dimensions were determined to be a length of 34.48 ± 0.01 µm, a width of 5.35 ± 0.01 µm, and an area of 21.68 ± 0.01 µm^2, two areas were analyzed using AFM to assess the crystal thickness.

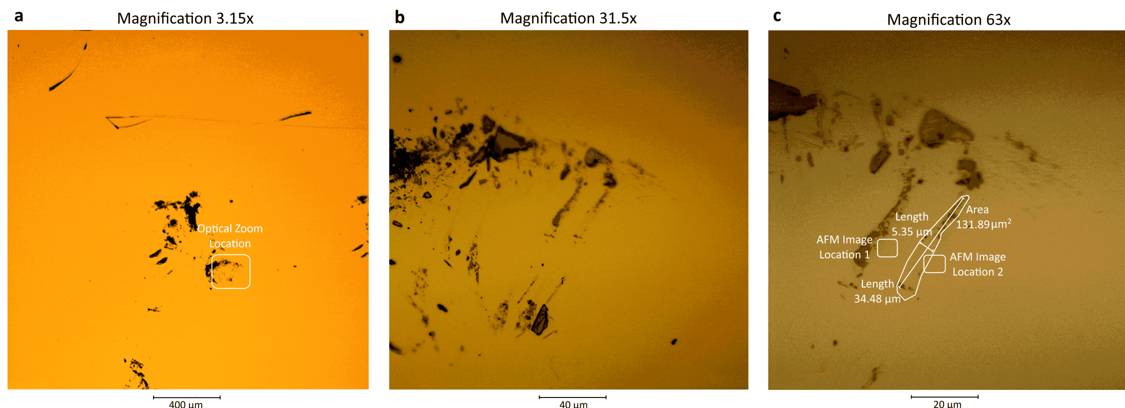

Figure 21: Optical microscope images of exfoliated $PtTe_2$ on Ag(111)/mica substrate at a) 3.15× magnification, b) 31.5× magnification, and c) 63× magnification with annotations indicating crystal length, width, and area.

The optical microscopy results show that the exfoliation of $PtTe_2$ yielded the smallest crystal, whereas exfoliation of $PtBi_2$ produced a crystal with the largest area. The limited exfoliation success of $PtTe_2$ may be attributed to the bulk crystal not being sufficiently flat or potentially buckled. Additionally, suboptimal exfoliation motion, with deviations from the ideal force and speed, may have reduced the exfoliation efficacy of this sample.

4.4 AFM Results

The optical microscope images show promising results for the exfoliation of the van der Waals crystals, the figures in Subsection 4.3 indicate the exact locations where the following AFM images were acquired for detailed height and structural analysis.

While not shown in this subsection, the magnification provided by AFM showed signs of water droplets on the sample's surface. XPS analysis confirmed the presence of water on the $Pt(BiTe)_2$ and $PtTe_2$ samples, as well as evidence of carbon impurities on all samples, the corresponding results are presented in Appendix C. This is important to note, as both moisture and carbon contaminants can influence the height measurements obtained via AFM and should therefore be considered when comparing these results to those reported in the literature. In the images presented in this subsection, a gold color pallet was chosen for its ability to maximize the contrast between the Ag(111)/mica and the exfoliated van der Waals crystals.

Firstly, the exfoliated $PtBi_2$ was examined using AFM. Figure 22a shows the first $20 \times 20\,\mu m$ scan, capturing the transition from the Ag(111)/mica substrate on the left to the monolayer $PtBi_2$ on the right. The sample shows no no sign of contamination, although a diagonal scratch is present on the sample in the $PtBi_2$ region. The area selected for higher magnification AFM imaging is marked in white, this image is displayed in Figure 22b using a scan size of $1 \times 1\,\mu m$. Small cylindrical features are visible, which may be water droplets or contamination caused by dust adsorption. Three line-scan height profiles were recorded across the transition region, the result of which are shown in Figure 22c, these profiles a monolayer step hight from $PtBi_2$ to the substrate of 1.3 ± 0.1 nm, 1.0 ± 0.1 nm, and 1.4 ± 0.1 nm for the red, black, and green line-scans, respectively.

These values are slightly larger than the reported $PtBi_2$ monolayer thickness of 0.60 nm discussed in Subsection 3.4, this hight discrepancy can be attributed to carbon impurities contaminating the sample's surface and instrumental offsets. The impact of these factors on height measurements is further evident from the variations in hight between the three measurements, despite the crystal appearing to have a uniform thickness.

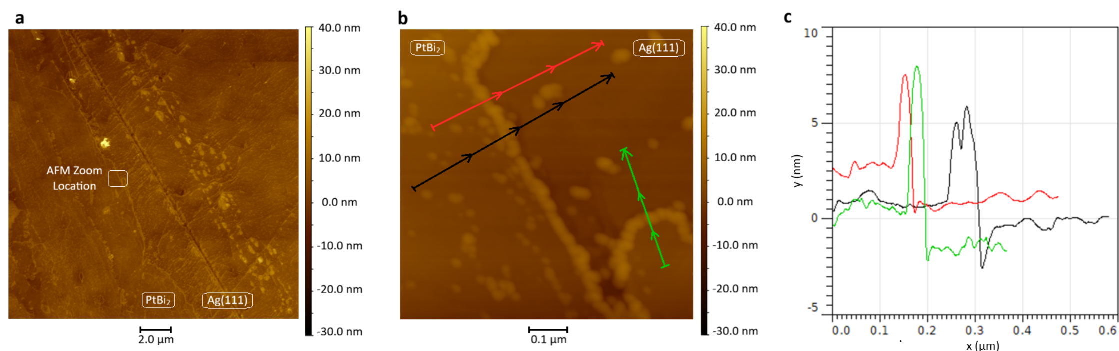

Figure 22: AFM results of the transition from $PtBi_2$ to Ag(111)/mica. Sample images are shown for a scan size of a) $20 \times 20\,\mu m$ and b) $1 \times 1\,\mu m$, with c) showing the corresponding line-scan height profile as a function of lateral distance.

An initial AFM scan of the sample containing $Pt(BiTe)_2$ crystals over an area of $20 \times 20\,\mu m$ shows the transition from the Ag(111) substrate to the $Pt(BiTe)_2$ crystal and is displayed Figure 23a, no surface contamination was observed. However, the image exhibits artifacts consistent with AFM tip damage, visible as sharp bright streaks that gradually fade toward the right side of the scan. This effect is marked using white circles around some of these artifacts in Figure 23b, which used a scan size of $8 \times 8\,\mu m$. The damaged AFM tip affected the accuracy of the measured height values, this problem can be reduced by increasing the width over which the measured high was averaged. The perpendicular markers at the ends of the height profile lines shows this width, with larger markers signify averaging over more measurements perpendicular to the line scan direction, reducing artifacts from tip damage. The result of the hight profile is shown in Figure 23c and determined the hight of this crystal to be $1.0 \pm 0.1\,nm$ for both the red and black line-scan taken.

Literature values for the thickness of monolayer $Pt(BiTe)_2$ are not available. Therefore, a comparison was made with the reported monolayer thicknesses of the structurally similar crystals $PtBi_2$ and $PtTe_2$, which have thicknesses of 0.60 nm and 0.522 nm, respectively, as reported in Subsection 3.4. The measured $Pt(BiTe)_2$ crystals have a slightly greater measured thickness than the reported monolayer values, this discrepancy can be attributed to the presence of carbon contaminants and surface moisture, as well as instrumental offset.

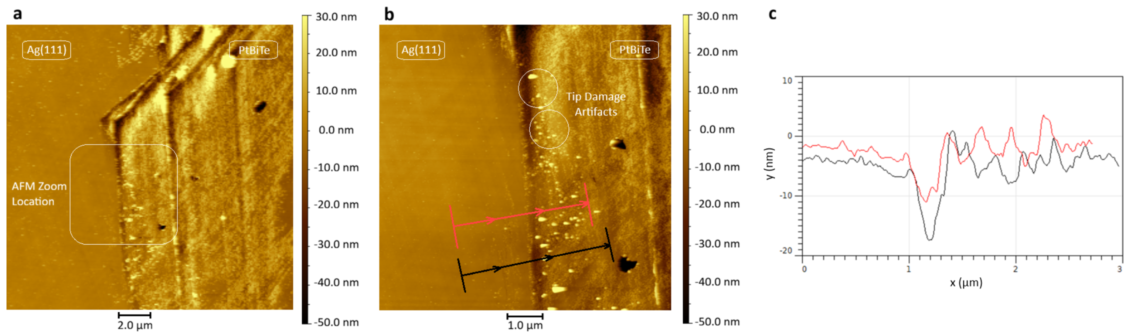

Figure 23: AFM results of the transition from Ag(111)/mica to $Pt(BiTe)_2$. Sample images are shown for a scan size of a) $20 \times 20\,\mu m$ and b) $8 \times 8\,\mu m$, with c) showing the corresponding line-scan height profile as a function of lateral distance.

The sample containing $PtTe_2$ was first scanned over an area of $20 \times 20\,\mu m$, as shown in Figure 24a, which highlights the region chosen for a more detailed scan. The resulting image of this selected area of $2 \times 2\,\mu m$ is shown in Figure 24b. Here, the transition from $PtTe_2$ is clearly visible and the Ag(111)/mica substrate exhibits terraced layers with flat regions separated by slightly rounded step edges, indicating non-uniform substrate growth not shown in other samples. The height of the $PtTe_2$ crystal was measured twice using line scans, with the results shown in Figure 24c. Both measurements indicate a $PtTe_2$ layer thickness of $1.3 \pm 0.1\,nm$.

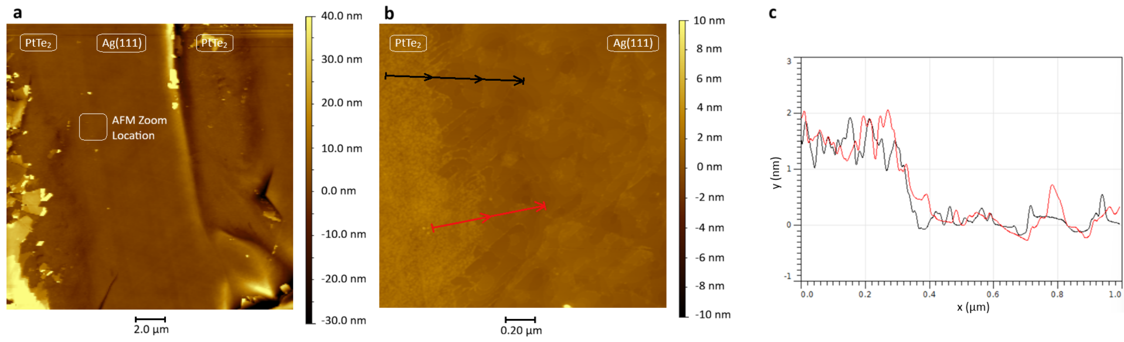

Figure 24: AFM results of the transition from Ag(111)/mica to $PtTe_2$ in spot 1. Sample images are shown for a scan size of a) $20 \times 20\,\mu m$ and b) $2 \times 2\,\mu m$, with c) showing the corresponding line scan height profile as a function of lateral distance.

This sample also was measured a second time, with the first scan covering an area of $30 \times 30\,\mu m$ shown in Figure 25a, this figure also indicates the region selected for the more detailed scan. This second measurement was performed over an area of $3 \times 3\,\mu m$, with the result shown in Figure 25b. The transition from $PtTe_2$ to the Ag(111)/mica substrate is clearly distinguishable, while the substrate again exhibits signs significant irregularities in height. Height measurements taken along the indicated hight measurement paths are plotted in Figure 25c, showing a $PtTe_2$ crystal height of 1.0 ± 0.1 nm.

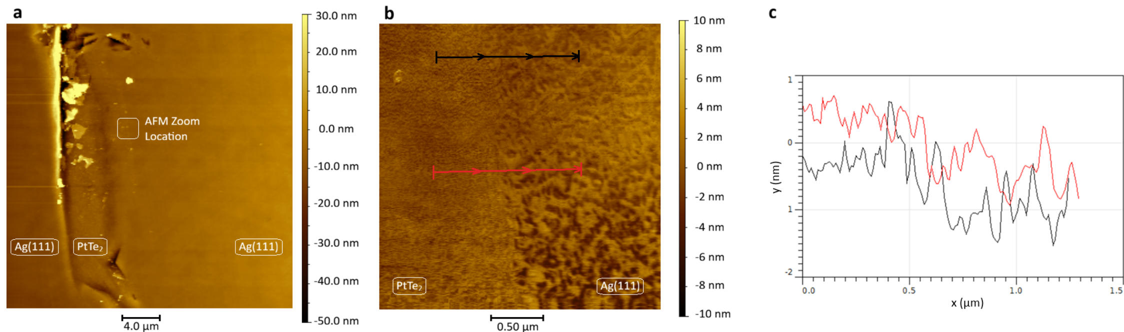

Figure 25: AFM results of the transition from Ag(111)/mica to $PtTe_2$ in spot 2. Sample images are shown for a scan size of a) $30 \times 30\,\mu m$ and b) $3 \times 3\,\mu m$, with c) showing the corresponding line scan height profile as a function of lateral distance.

The measured heights of crystals on this substrate exceed the $PtTe_2$ monolayer thickness of 0.522 nm reported in literature, discussed in Subsection 3.4. These slight deviations from the values reported in literature likely arise from the presence of carbon contaminants, surface moisture, and instrumental offset.

To summarize, the measured crystal heights of all samples consistently exceeded the corresponding monolayer values reported in the literature. Nevertheless, the crystal heights measured are still well below the height expected for bilayer crystals, which would need to be significantly more than twice the reported monolayer value to account for surface contamination and instrumental offset. These observations indicate that the flakes measured are indeed monolayer crystals.

4.5 XPS Results

Information on the composition and chemical states of exfoliated materials is obtained through XPS. Due to the relatively large size of the X-ray beam it is not possible to probe only the monolayers, therefore all XPS results correspond to measurements of the complete exfoliation sites previously discussed. The samples were exposed to ambient conditions and were not annealed prior to the XPS measurements. Furthermore, the intensity of the peaks shown in this subsection are proportional to the number of electrons emitted after X-ray absorption, to identify each peak its binding energy was compared to literature.

A wide scan survey spectrum was used to measure the intensity of core-level electrons as a function of binding energy over a range of -10 to 850 eV. The wide scan provide a general overview of materials present at the exfoliation site and can indicate the materials that have contaminated the sample. Furthermore, high-resolution scans are shown to offer information regarding crystal crystal composition and potential oxidation states. Additionally, the higher resolution enables the detection of metals with peaks that are significantly less intense than those of other materials, and provide more precise information regarding the degree of contamination.

The initial XPS wide scan results indicate that the exfoliation site of the first sample contains $PtBi_2$, as shown in Figure 26. The spectrum clearly displays the core-level peaks of platinum, bismuth, and silver. The prominent silver peaks arise from the silver substrate, and air exposure during the transfer from the exfoliation vacuum chamber to the XPS chamber led to the appearance of oxygen and carbon peaks. The sulfide peaks indicate sulfide was also present on the sample, although exact origin of the sulfide is unknown it may have arisen from airborne contamination, adsorption from ambient dust, or vacuum grease of the LEED system containing sulfide additives.

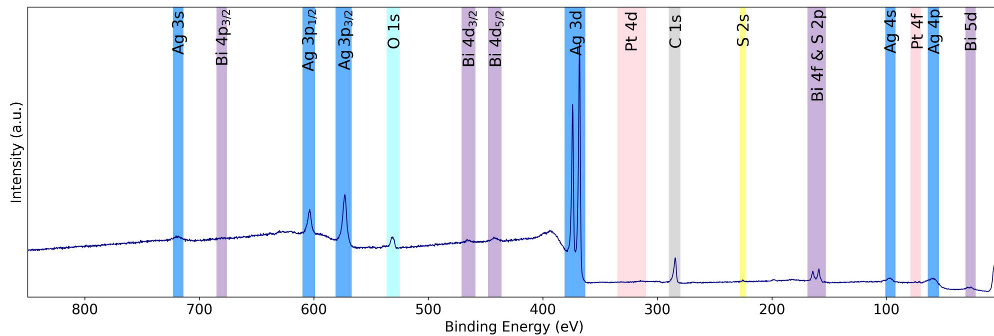

Figure 26: XPS wide scan of the $PtBi_2$ exfoliation site on Ag(111)/mica, showing intensity as a function of binding energy, peaks of core-level electronic states are shaded.

The second sample analyzed was found to contain $Pt(BiTe)_2$, as shown in Figure 27. The silver peaks remain prominent as a result of the silver substrate. Platinum and bismuth peaks from the exfoliated crystal are detected, although they appears with low intensity. The tellurium peaks are not clearly distinguishable in the wide-scan spectrum, since the only resolvable tellurium signal is the Te 3d peak and it overlaps with the much stronger Ag $3p_{3/2}$ core-level. Nevertheless, a narrow-scan analysis can confirm the presence of tellurium at the exfoliation site. Oxygen and carbon peaks are again observed, consistent with the previously discussed exposure effects from the ambient entremets during transfer. Sulfide is again detected in this sample, indicating that sulfide

contamination in the laboratory environment is either systematic or originates from the air.

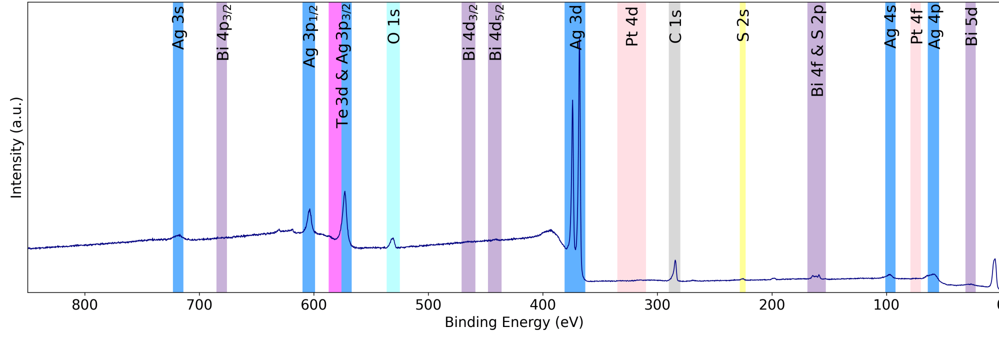

Figure 27: XPS wide scan of the $Pt(BiTe)_2$ exfoliation site on Ag(111)/mica, showing intensity as a function of binding energy, peaks of core-level electronic states are shaded.

The wide scan result of the final sample is presented in Figure 28. Silver core-level peaks from the substrate are clearly visible, and low intensity platinum peaks from the exfoliated van der Waals crystal are also detected. The tellurium signal overlaps with the silver $3p_{3/2}$ peak, thus requiring high resolution XPS to be resolved. Additionally, oxygen and carbon peaks are observed, arising from exposure to the ambient environment during sample transfer.

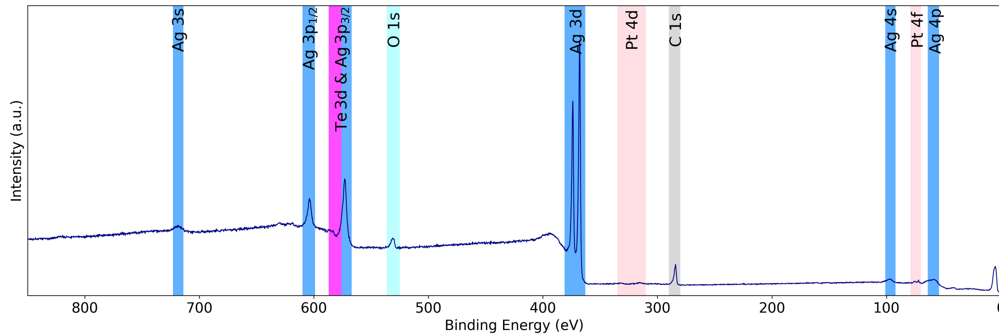

Figure 28: XPS wide scan of the $PtTe_2$ exfoliation site on Ag(111)/mica. Showing intensity as a function of binding energy, peaks of core-level electronic states are shaded.

Various binding energy regions in the spectra of each sample were examined using high-resolution XPS scans, this section presents and discusses the spectra that are central to this research, supplementary narrow scans are provided in Appendix C. The minimum resolvable peak width is given by $\Delta_{\text{peak}} = \frac{\text{Resolution}}{\sqrt{N_{\text{scans}}}}$, where the instrumental resolution is 1.3 eV and N_{scans} corresponds to the number of scans used to acquire the spectrum, which was either three or four depending on the sample. Additionally, the peaks separation can also not be smaller than the value of Δ_{peak}.

High resolution Pt 4f core-level scans of the $PtBi_2$, $Pt(BiTe)_2$, and $PtTe_2$ exfoliation sites are depicted in Figures 29a, 29b, and 29c, respectively. Each fit includes a Shirley background shown by the dashed line. Note that the small size of the $Pt(BiTe)_2$ produced a low XPS signal, giving rise to a high signal-to-noise ratio on the low binding energy side. The violet line corresponds to the Pt 4f core-level metallic bond with either bismuth or tellurium.

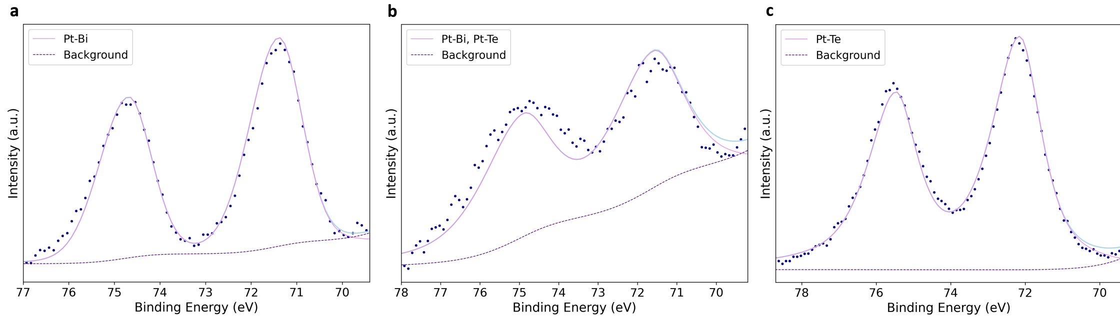

Figure 29: XPS narrow scan of the Pt 4f core-level, showing intensity as a function of binding energy of Ag(111)/mica with exfoliated a) $PtBi_2$, b) $Pt(BiTe)_2$, and c) $PtTe_2$.

The peak position and spin-orbit splitting of the measured Pt 4f spectral peak are compared with values from literature, as summarized in Table 1. The reported literature values correspond to bulk $PtTe_2$, which has a different chemical environment in 2D $PtBi_2$, $Pt(BiTe)_2$, and $PtTe_2$.

Despite these differences, the measured spin-orbit splitting of all samples is consistent with values reported in literature within the margin of error. The measured Pt 4f peak position of $PtTe_2$ also agree with the value reported in literature. In contrast, the observed Pt 4f peak positions of the samples containing bismuth do not coincide that of literature, this is the result of differences in chemical environment between the samples and literature. As this difference is increased, by introducing more bismuth, the peak position of the pt 4f also deviates further from the peak position reported in literature.

	Peak Position (eV)	Spin-Orbit Splitting (eV)
$PtBi_2$	71.4 ± 0.7	3.3 ± 0.7
$Pt(BiTe)_2$	71.6 ± 0.8	3.3 ± 0.8
$PtTe_2$	72.2 ± 0.7	3.3 ± 0.7
Literature (Bulk $PtTe_2$)[62]	72.5 ± 0.1	3.33 ± 0.01

Table 1: Pt 4f core-level XPS peak positions and spin-orbit splitting of the measured samples and literature.

Furthermore, the high resolution scans bismuth 4f core-level of the exfoliation sites containing $PtBi_2$, and $Pt(BiTe)_2$ are displayed in Figures 30a, and 30b, respectively. Both fits include a Shirley background indicated by the dashed line. The asymmetric green peaks show the metallic bond of bismuth to platinum (Bi-Pt). The symmetric pink peaks correspond to single bismuth oxygen bonds (Bi-O), and indicate the material is partially oxidized. The dark red symmetric peaks correspond to bismuth double bonded to oxygen (Bi=O), and indicate the presence of oxygenated bismuth at the surface.

Additionally, a sulfide 2p signal is observed in the $PtBi_2$ and $Pt(BiTe)_2$ samples, this signal is indicated by the asymmetric yellow peak. The positions of these peaks are located at 161.21 ± 0.7 eV for $PtBi_2$ and 161.21 ± 0.8 eV for $Pt(BiTe)_2$, which are in agreement with the theoretical value of 162 ± 2 eV.[50]. The wide scan XPS spectra shown in Figures 26 and 27 also show a sulfide 2s peak near 225 eV, matching the value of 225 eV reported in theory value.[50] thus confirming the presence of sulfide on both samples. This suggests the presence of a sulfide contamination source in the laboratory environment or in the surrounding air.

Sulfide is in the -2 oxidation state and bound to metals, in these samples it can be bounded to silver or to any of the metals in the van der Waals crystals that were exfoliated, creating Ag-S, Pt-S, Bi-S, and Te-S bonds. The core-level peak positions of these bonds are too close to be distinguished in the figures shown, however since silver is the most abundant metal in the samples most of the sulfide is likely bound to silver creating a large amount of Ag-S bonds.

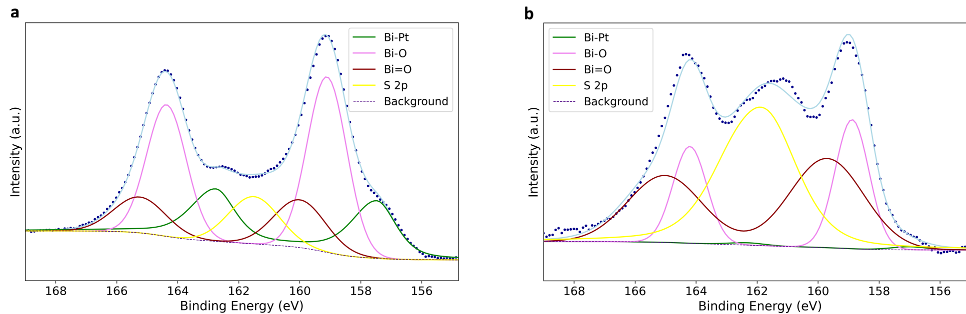

Figure 30: XPS narrow scan of the Bi 4f core-level, showing intensity as a function of binding energy of Ag(111)/mica with exfoliated a) $PtBi_2$, b) $Pt(BiTe)_2$.

Lastly, Table 2 summarizes the peak positions and spin-orbit splitting for the $PtBi_2$ and $Pt(BiTe)_2$ exfoliation sites. Although the literature values listed in the table were obtained in chemical environments different from those experienced by bismuth in 2D $PtBi_2$ and $Pt(BiTe)_2$, the measured peak positions and spin-orbit splitting are within the reported margins of error.

	Peak Position (eV)	Bi-O Position (eV)	Bi=O Position (eV)	S-O Splitting (eV)
$PtBi_2$	157.6 ± 0.7	159.1 ± 0.7	160.0 ± 0.7	5.3 ± 0.7
$Pt(BiTe)_2$	157.0 ± 0.8	158.9 ± 0.8	159.7 ± 0.8	5.3 ± 0.8
Literature (Bulk Bi-Te)[50, 63]	157.1 ± 0.3	159.5 ± 0.3	160.0 ± 0.1	5.31 ± 0.01

Table 2: Bi 4f XPS peak positions, oxidation position, spin-orbit splitting, and chemical shift for the measured samples and literature.

Finally, high resolution scans in the Te 3d core-level domain of the exfoliation sites containing $Pt(BiTe)_2$, and $PtTe_2$ are shown in Figures 37a, 37b. Due to the low signal-to-noise ratio, the tellurium sample required a linear background, while the $PtTe_2$ sample used a Shirley background, both figures used a dashed line to indicate background noise. Metallic tellurium bonded to platinum (Te–Pt) is represented by an asymmetric pink peak, whereas oxidized tellurium (Te–O) is shown as a symmetric peak using a green line in the figures.

When measuring the signal intensity of the $Pt(BiTe)_2$ sample, the binding energy range was shortened to prevent interference from the nearby Ag 3p peak. This change allowed the Te $3d_{3/2}$ peak to be resolved and was required due to time constraints. Consequently, spin-orbit splitting could not be measured in this sample. For the $PtTe_2$ sample, this reduction in binding energy range was not necessary, allowing spin-orbit splitting to be measured, this binding energy range also made the the asymmetric red Ag 3p peak clearly visible.

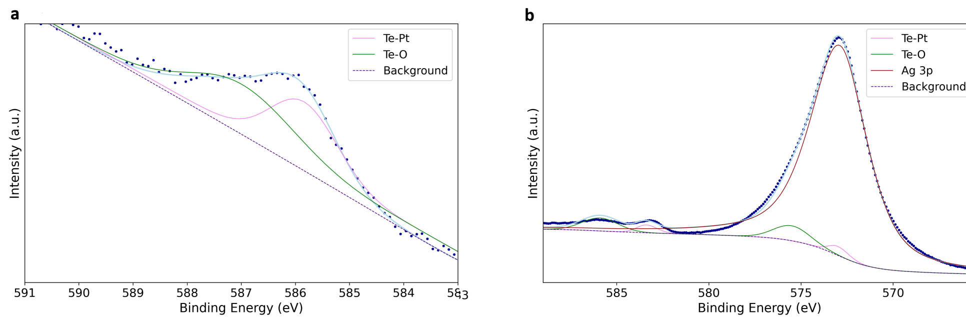

Figure 31: XPS narrow scan of the Te 3d core-level, showing intensity as a function of binding energy of Ag(111)/mica with exfoliated a) $Pt(BiTe)_2$, b) $PtTe_2$.

The relevant peak positions and measured spin–orbit splitting were determined and compared with corresponding literature values, summarized in Table 3. The peak position for $Pt(BiTe)_2$ does not exactly match the literature value, which may have been caused by differences in the chemical environment of the sample compared to that of the reported literature data. All other measured values are consistent with those reported in the literature.

	Position Te-Pt $3d_{3/2}$ (eV)	Position Te-O $3d_{3/2}$ (eV)	S-O Splitting (eV)
$Pt(BiTe)_2$	585.8 ± 0.8	587.0 ± 0.8	—
$PtTe_2$	583.4 ± 0.7	585.9 ± 0.7	10.4 ± 0.7
Literature (Bulk $PtTe_2$)[50]	583.4 ± 0.3	586.4 ± 0.2	10.39 ± 0.01

Table 3: Te 3d XPS peak positions, oxidation position, spin-orbit splitting, and chemical shift for the measured samples and literature.

The high resolution XPS data was further analyzed by determining the normalized area of each peak, obtained by dividing the area under each curve by the sensitivity factor of that chemical environment. These normalized areas were then used to calculate the atomic percentages, providing even more information on each chemical environment, these results are summarized in Tables 4, 5, and 6 in Appendix D.

This data reveal some notable trends. In particular, the $PtBi_2$, $Pt(BiTe)_2$, and $PtTe_2$ samples exhibit atomic ratios of Pt:Bi $= 6.3 \pm 0.7$, Pt:(Bi+Te) $= 2.2 \pm 0.3$, and Pt:Te $= 0.007 \pm 0.001$, respectively. The extremely low Pt:Te ratio indicates that very little telluride is present in the exfoliated crystals. The three ratios show that as the bismuth concentration in the source crystal decreases and telluride concentration increases, the amount of telluride in the exfoliated crystal substantially decreases.

This result was certainly not expected and represents a phenomenon for which there is no prior literature to fall back on. To explain the results, one can consider the potential exfoliation behavior of $PtTe_2$. A monolayer $PtTe_2$ consists of a Pt layer which is sandwiched between two layers of tellurium, during the exfoliation of this van der Waals crystal it is possible that only the bottom tellurium layer along with the central platinum layer remained on the substrate, while the top layer of tellurium was removed. In this arrangement, the platinum layer positioned above the bottom tellurium layer could have acted as an X-ray-absorbing barrier, potentially hindering the core-level measurements from detecting the underlying tellurium.

Lastly, the ratio of bismuth to tellurium in the exfoliated $Pt(BiTe)_2$ crystal can be

determined using the formula (Bi(0) + Bi-O)/(Te-Pt + Te-O) = 1.6, which corresponds to an elemental composition of $PtBi_xTe_{1-x}$, with $x \approx 0.6$.

In summary, KISS exfoliation successfully produced monolayer $PtBi_2$, $Pt(BiTe)_2$, and $PtTe_2$ crystals on Ag(111)/mica. Optical microscopy determined the surface area of the exfoliated $PtBi_2$ crystals to be the largest, whereas the $PtTe_2$ flakes exhibited the smallest surface area. AFM measurements confirmed the crystal thicknesses to be consistent with theoretical monolayer values when taking into account substrate contamination and the instrumental offset of the AFM. Furthermore, LEED analysis verified the presence of an exfoliated $Pt(BiTe)_2$ flake on the substrate, with its domain rotated $26.06 \pm 0.08°$ with respect to the Ag(111)/mica crystal. Lastly, high-resolution XPS verified the presence of each van der Waals crystal at their respective exfoliation sites.

5 Discussion

5.1 The Impact of Vacuum System Modifications

The proposed modifications to the vacuum system designed in FreeCAD have the potential to improve the overall exfoliation process, by modifying the manipulator arm to anneal multiple samples simultaneously, combined with active substrate cooling, preparation time can reduced. While simultaneous sputtering was considered, the alignment of multiple guns may limit efficiency improvement. It should be noted that these approaches aim to improve throughput and do not enhance the effectiveness of exfoliation. Furthermore, restricting the transfer arm to translational motion along the x-axis possible improves consistency, although further optimization is needed as the bulk crystal holder can still shift, reducing exfoliation reproducibility.

Finally, the addition of a dedicated measurement chamber adjacent to the preparation chamber could enable *in situ* measurements and improve sample visibility through extra viewing gaskets, although the effect of increased visibility on exfoliation efficacy is unclear and remains to be investigated.

5.2 Critical Assessment of the Exfoliation Result

The van der Waals crystals $PtBi_2$, $Pt(BiTe)_2$, and $PtTe_2$ were successfully exfoliated on Ag(111)/mica via KISS. Using optical microscopy, the crystals selected for further analysis were measured to have lengths and widths of $211.4 \pm 0.01\mu m \times 114.45 \pm 0.01\mu m$, $113.65 \pm 0.01\mu m \times 20.65 \pm 0.01\mu m$, and $34.48 \pm 0.01\mu m \times 5.35 \pm 0.01\mu m$. The crystals were found to have areas of $20028.12 \pm 0.01\mu m^2$, $2129.68 \pm 0.01\mu m^2$, and $131.89 \pm 0.01\mu m^2$. They were slightly uneven in thickness, and located near bulk.

Only $Pt(BiTe)_2$ on Ag(111)/mica exhibited sufficient size and long-range order for a clear LEED signal to be detected. The resulting LEED patterns were hexagonal, with the Ag(111) pattern appearing 45 % larger than the faint hexagonal pattern of $Pt(BiTe)_2$, this value exceeds the theoretically predicted value of 39 % discussed in Subsection 3.1. The deviation of 6 % is likely caused by experimental factors, such as the sample surface not being perfectly flat and the electron gun not being perfectly perpendicular to the sample's surface. Lastly, the crystal unit cells were oriented at $26.06 \pm 0.08°$ relative to each other. Future work should focus on crystals with improved uniformity, flatness and long-range order for more consistent LEED patterns.

AFM measurements of the $PtBi_2$ crystal showed thicknesses of 1.0 ± 0.1 nm, 1.3 ± 0.1 nm, and 1.4 ± 0.1 nm depending on the location of the measurement. The $Pt(BiTe)_2$ crystal exhibited a thickness of 1.3 ± 0.1 nm, while the $PtTe_2$ crystal was found to have a thickness of 1.0 ± 0.1 nm. The crystal height exceed the monolayer thickness reported in literature for each crystal measured,[21, 60] likely caused by carbon contamination, surface moisture, and AFM instrumental offset. Despite this, the measured crystal heights remain below those expected for bilayer, confirming the flakes are monolayers. Line scans across the substrate-crystal interface showed significant height variability, indicating that selecting optimal measurement sites could improve analysis precision.

High resolution XPS scan of the samples containing $PtBi_2$, $Pt(BiTe)_2$, and $PtTe_2$ showed a Pt 4f core-level signal with peak positions of 71.4 ± 0.7 eV, 71.6 ± 0.8 eV, and 72.2 ± 0.7 eV, respectively. The spin-orbit splitting of these peaks was measured to be 3.3 ± 0.7 eV, 3.3 ± 0.8 eV, and 3.3 ± 0.7 eV. With the exception of the peaks from $PtBi_2$ and $Pt(BiTe)_2$, the measured values agree with the literature values for bulk $PtTe_2$, which has a peak position of 72.5 ± 0.1 eV and a spin-orbit splitting of 3.33 ± 0.1 eV.[62] Furthermore, the samples containing $PtBi_2$ and $Pt(BiTe)_2$ exhibit a Bi 4f core-level peak at 157.6 ± 0.7 eV and 157.0 ± 0.8 eV, with a spin-orbit splittings of 5.3 ± 0.7 eV and 5.3 ± 0.8 eV, respectively. These values are in agreement with values from literature for bulk Bi-Te, which report a peak position of 157.1 ± 0.3 eV and a spin-orbit splitting of 5.31 ± 0.01 eV.[50, 63] Lastly, high resolution XPS of the $Pt(BiTe)_2$ and $PtTe_2$ crystals revealed a Te $3d_{3/2}$ core-level peak at 585.8 ± 0.8 eV and 583.4 ± 0.7 eV, respectively. The spin-orbit splitting for the $Pt(BiTe)_2$ sample could not be determined due to time constraints, while the $PtTe_2$ sample showed a Te 3d splitting of 10.4 ± 0.7 eV. Literature values for bulk $PtTe_2$ report a peak position of 583.4 ± 0.3 eV and a splitting of 10.39 ± 0.01 eV.[50] The differences in peak position from literature is attributed to the differences in chemical environment between the measured crystals and the material from literature it was compared to, highlighting the currently limited reference data for these 2D materials and the need for further research on these materials to allow for more accurate comparisons to be made.

Furthermore, S 2p signals in $PtBi_2$ and $Pt(BiTe)_2$ samples originating from sulfide bound to the silver substrate indicated that a more inert substrate, such as Au(111)/mica, could help limit sulfide adsorption. The XPS analysis revealed that the $PtBi_2$ crystal had a Pt:Bi atomic ratio of 6.3 ± 0.7, $Pt(BiTe)_2$ exhibited a Pt:(Bi+Te) ratio of 2.2 ± 0.3, and $PtTe_2$ showed a Pt:Te ratio of 0.007 ± 0.001. This unexpected result may be caused by the exfoliation behavior of $PtTe_2$, where the top tellurium layer of the monolayer was removed during exfoliation, the remaining platinum layer above the bottom tellurium acted as an X-ray-absorbing barrier, hindering the core-level XPS analysis of the tellurium. Lastly, XPS analysis of $PtBi_xTe_{1-x}$ indicated a composition of $x \approx 0.6$. In general, XPS measurements were limited by a low signal-to-noise ratio due to the relatively small size of the exfoliated crystals on the silver substrate, and by an XPS spot size too large to isolate individual monolayers, resulting in signal contributions from the sample and surrounding bulk material.

Ultimately, the number of exfoliation attempts in this research was limited, additional attempts in future would work result in more conclusive results. Nevertheless, the exploratory results demonstrate the potential of KISS, indicating it can successfully exfoliate large area monolayer $PtBi_2$, $Pt(BiTe)_2$, and $PtTe_2$ crystals onto Ag(111)/mica substrate.

6 Conclusion

The UHV KISS chamber was modeled in FreeCAD to visualize and assess potential design modifications aimed at improving the KISS exfoliation process. These changes include enabling simultaneous substrate annealing and cooling to shorten substrate preparation time, restricting transfer arm movement to the direction of exfoliation to enhance consistency, and adding a dedicated measurement chamber for the *in situ* integration of LEED, XPS, AFM, and optical microscopy in UHV.

In conclusion, the discussed modifications demonstrate UHV design changes can potentially mitigate key limitations of the exfoliation process, while further research needed to combine and evaluate these design approaches to guide further KISS UHV system improvements.

KISS exfoliation of $PtBi_2$, $Pt(BiTe)_2$, and $PtTe_2$ onto clean Ag(111)/mica substrates was carried out under UHV conditions. Optical microscopy results indicated the exfoliated $PtBi_2$ crystals possessed the largest surface area, $Pt(BiTe)_2$ crystals were of intermediate size, with $PtTe_2$ flakes being the smallest. AFM measurements confirmed the crystal thicknesses to be consistent with theoretical monolayer values when taking into account contamination and the instrumental offset of the AFM. LEED identified $Pt(BiTe)_2$ on the substrate after the exfoliation, indicated by two weak spots from its hexagonal diffraction pattern, alongside a 45 % larger hexagonal pattern originating from the silver substrate. The patterns were rotated by $26.06 \pm 0.08°$ relative to each other. Lastly, XPS analysis confirmed the presence of the Pt 4f peak at all exfoliation sites, the Bi 4f peak was observed at the $PtBi_2$ and $Pt(BiTe)_2$ sites, and the Te 3d signal was detected at the $Pt(BiTe)_2$ and $PtTe_2$ sites. The measured peak positions and spin-orbit splittings coincide with values reported in literature, with the exception position of the Pt 4f peak in bismuth-containing samples and the Te 3d peak in $Pt(BiTe)_2$.

In conclusion, the results demonstrated the potential of KISS to effectively produce large-area mono- and multilayer $PtBi_2$, $Pt(BiTe)_2$, and $PtTe_2$ crystals on Ag(111)/mica substrates.

References

[1] Erik Huss. *Nobel Prize in Physics 2010*. Oct. 2010. URL: https://www.nobelprize.org/prizes/physics/2010/press-release.

[2] Qing Lin He et al. “Topological spintronics and magnetoelectronics”. In: *Nature Materials* 21 (Jan. 2022), pp. 15–23. ISSN: 1476-4660. DOI: 10.1038/s41563-021-01138-5.

[3] Haifeng Tang et al. “Giant Planar Hall Effect in Epitaxial (Ga, Mn)As Devices”. In: *Physical Review Letters* 90.10 (Mar. 2003), pp. 107201–4. ISSN: 0031-9007. DOI: 10.1103/PhysRevLett.90.107201.

[4] Yuan Huang et al. “Universal mechanical exfoliation of large-area 2D crystals”. In: *Nature Communications* 11.2453 (May 2020), p. 2453. ISSN: 2041-1723. DOI: 10.1038/s41467-020-16266-w.

[5] Antonija Grubišić-Čabo et al. “In Situ Exfoliation Method of Large-Area 2D Materials”. In: *Advanced Science* 10.22 (Aug. 2023), p. 2301243. ISSN: 2198-3844. DOI: 10.1002/advs.202301243.

[6] Zhiying Dan et al. "Role of chalcogen atoms in in situ exfoliation of large-area 2D semiconducting transition metal dichalcogenides". In: *Frontiers in Nanotechnology* Volume 7 - 2025 (2025). ISSN: 2673-3013. DOI: 10.3389/fnano.2025.1553976.

[7] Xiang Ni et al. "Topological Metamaterials". In: *Chemical Reviews* 123.12 (June 2023), pp. 7585–7654. ISSN: 0009-2665. DOI: 10.1021/acs.chemrev.2c00800.

[8] Gui-Geng Liu et al. "Localization of Chiral Edge States by the Non-Hermitian Skin Effect". In: *Physical Review Letters* 132.11 (Mar. 2024), p. 113802. DOI: 10.1103/PhysRevLett.132.113802.

[9] Charles Kane. "Topological Band Theory and the $\mathbb{Z}_2$ Invariant". In: *Contemporary Concepts of Condensed Matter Science*. Vol. 6. Elsevier, Jan. 2013, pp. 3–34. DOI: 10.1016/B978-0-444-63314-9.00001-9.

[10] Ruikuan Xie et al. "Progress, Advantages, and Challenges of Topological Material Catalysts". In: *Small Science* 2.4 (Feb. 2022). ISSN: 2688-4046. DOI: 10.1002/smsc.202100106.

[11] Mingzhe Yan et al. "Lorentz-violating type-II Dirac fermions in transition metal dichalcogenide $PtTe_2$". In: *Nature Communications* 8.257 (Aug. 2017), p. 257. ISSN: 2041-1723. DOI: 10.1038/s41467-017-00280-6.

[12] Wenzhuo Zhuang and Zhongqiang Chen. "Large-area fabrication of 2D layered topological semimetal films and emerging applications". In: *Advances in Physics: X* 7.1 (Dec. 2022). ISSN: 2374-6149. DOI: 10.1080/23746149.2022.2034529.

[13] Alan Kostelecký et al. "Lorentz violation in Dirac and Weyl semimetals". In: *Physical Review Research* 4.2 (May 2022), p. 023106. DOI: 10.1103/PhysRevResearch.4.023106.

[14] Frank Schindler et al. "Higher-order topological insulators". In: *Science Advances* 4.6 (June 2018). ISSN: 2375-2548. DOI: 10.1126/sciadv.aat0346.

[15] Yoshimasa Hidaka, Ken Shiozaki, and Kenji Fukushima. "Symmetry protected topological phases of matter". In: *Progress of Theoretical and Experimental Physics* 2022.4 (Apr. 2022), 04A001. ISSN: 2050-3911. DOI: 10.1093/ptep/ptac049.

[16] Ke Deng et al. "Crossover from 2D metal to 3D Dirac semimetal in metallic $PtTe_2$ films with local Rashba effect". In: *Science Bulletin* 64.15 (Aug. 2019), pp. 1044–1048. ISSN: 2095-9273. DOI: 10.1016/j.scib.2019.05.023.

[17] Grigory Shipunov et al. "Polymorphic $PtBi_2$: Growth, structure, and superconducting properties". In: *Physical Review Material* 4.12 (Dec. 2020), p. 124202. DOI: 10.1103/PhysRevMaterials.4.124202.

[18] Sebastian Schimmel et al. "Surface superconductivity in the topological Weyl semimetal t-$PtBi_2$". In: *Nature Communications* 15.9895 (Nov. 2024), p. 9895. ISSN: 2041-1723. DOI: 10.1038/s41467-024-54389-6.

[19] Grigory Shipunov et al. "Polymorphic $PtBi_2$: Growth, structure and superconducting properties". In: *Physical Review Materials* (Feb. 2020). DOI: 10.1103/PhysRevMaterials.4.124202.

[20] Meng-Kai Lin et al. "Dimensionality-Mediated Semimetal-Semiconductor Transition in Ultrathin $PtTe_2$ Films". In: *Physical Review Letters* 124.3 (Jan. 2020), p. 036402. DOI: 10.1103/PhysRevLett.124.036402.

[21] Xiao-Ang Nie et al. "Robust Hot Electron and Multiple Topological Insulator States in $PtBi_2$". In: *American Chemical Society Nano* 14.2 (Feb. 2020), pp. 2366–2372. ISSN: 1936-0851. DOI: 10.1021/acsnano.9b09564.

[22] Luqiao Liu et al. "Spin-Torque Switching with the Giant Spin Hall Effect of Tantalum". In: *Science* 336.6081 (May 2012), pp. 555–558. ISSN: 0036-8075. DOI: 10.1126/science.1218197.

[23] Alex R. Mellnik et al. "Spin-transfer torque generated by a topological insulator". In: *Nature* 511 (July 2014), pp. 449–451. ISSN: 1476-4687. DOI: 10.1038/nature13534.

[24] Haijun Zhang, Chao-Xing Liu, and Shou-Cheng Zhang. "Spin-Orbital Texture in Topological Insulators". In: *Physical Review Letters* 111.6 (Aug. 2013), p. 066801. DOI: 10.1103/PhysRevLett.111.066801.

[25] Kouta Kondou et al. "Fermi-level-dependent charge-to-spin current conversion by Dirac surface states of topological insulators". In: *Nature Physics* 12 (Nov. 2016), pp. 1027–1031. ISSN: 1745-2481. DOI: 10.1038/nphys3833.

[26] Muthuvel M. Raja et al. "Thermal sprayed thick-film anisotropic magnetoresistive sensors". In: *Institute of Electrical and Electronics Engineers Transactions on Magnetics* 40.4 (July 2004), pp. 2685–2687. DOI: 10.1109/TMAG.2004.832249.

[27] Wei Ai et al. "Observation of giant room-temperature anisotropic magnetoresistance in the topological insulator β-Ag_2Te". In: *Nature Communications* 15.1259 (Feb. 2024), pp. 1–9. ISSN: 2041-1723. DOI: 10.1038/s41467-024-45643-y.

[28] Luiz G. Enger et al. "Sub-nT Resolution of Single Layer Sensor Based on the AMR Effect in La2/3Sr1/3MnO3 Thin Films". In: *Institute of Electrical and Electronics Engineers Transactions on Magnetics* 58.2 (June 2021). DOI: 10.1109/TMAG.2021.3089373.

[29] Ming-Xun Deng et al. "Competing effects of magnetic impurities in the anomalous Hall effect on the surface of a topological insulator". In: *Physical Review B* 94.23 (Dec. 2016), p. 235116. DOI: 10.1103/PhysRevB.94.235116.

[30] Luca Bignardi et al. "Growth and structure of singly oriented single-layer tungsten disulfide on Au(111)". In: *Progress in Surface Science* 3.1 (Jan. 2019), p. 014003. DOI: 10.1103/PhysRevMaterials.3.014003.

[31] Fang Liu. "Mechanical exfoliation of large area 2D materials from vdW crystals". In: *Progress in Surface Science* 96.2 (May 2021), p. 100626. ISSN: 0079-6816. DOI: 10.1016/j.progsurf.2021.100626.

[32] Won Kang et al. "Direct growth of doping controlled monolayer WSe2 by selenium-phosphorus substitution". In: *Nanoscale* 10.24 (June 2018), pp. 11397–11402. ISSN: 2040-3364. DOI: 10.1039/C8NR03427C.

[33] Xisai Zhang et al. "Advanced tape-exfoliated method for preparing large-area 2D monolayers: a review". In: *2D Materials v8 n3 (20210701)* (2021). ISSN: 2053-1583. DOI: 10.1088/2053-1583/ac016f.

[34] Prachi Budania et al. "Comparison between Scotch tape and gel-assisted mechanical exfoliation techniques for preparation of 2D transition metal dichalcogenide flakes". In: *Micro and Nano Letters* 12.12 (Dec. 2017), pp. 970–973. ISSN: 1750-0443. DOI: 10.1049/mnl.2017.0280.

[35] Philip Hofmann. *Surface Physics, An Introduction.* Self-Published, 2013. ISBN: 978-87-996090-1-7.

[36] Vac Aero International. *Oil Sealed Rotary Vane Pumps.* Jan. 2020. URL: https://vacaero.com/information-resources/vacuum-pump-technology-education-and-training/195875-oil-sealed-rotary-vane-pumps.html.

[37] Zhi Chen et al. "Modeling and Optimization of the Blade Structural Parameters for a Turbomolecular Pump". In: *Machines* 11.5 (May 2023), p. 517. ISSN: 2075-1702. DOI: 10.3390/machines11050517.

[38] John F. O'Hanlon and Timothy A. Gessert. *Turbomolecular Pumps*. Winley Semiconductors, 2024. DOI: 10.1002/9781394174232.ch11.

[39] Sunit. Sindal et al. "Development and UHV testing of LN2 cooled Titanium Sublimation Pump". In: *Journal of Physics: Conference Series* 390 (Nov. 2012). DOI: 10.1088/1742-6596/390/1/012022.

[40] Vac Aero International. *Proper Selection and Use of Vacuum Gauges*. Feb. 2019. URL: https://vacaero.com/information-resources/vacuum-pump-technology-education-and-training/192176-proper-selection-and-use-of-vacuum-gauges.html.

[41] Arun Microelectronics Ltd. *How does an ion gauge work?* Feb. 2022. URL: https://www.arunmicro.com/news/how-does-an-ion-gauge-work/.

[42] Tomasz Grzela. "Comparative STM-based study of thermal evolution of Co and Ni germanide nanostructures on Ge(001)". PhD thesis. Poznan University of Technology, Dec. 2015.

[43] Yongjun Huo and Jiaqi Wu. "Solid solution softening and enhanced ductility in concentrated FCC silver solid solution alloys". In: *Materials Science and Engineering: A* 729 (June 2018), pp. 208–218. ISSN: 0921-5093. DOI: 10.1016/j.msea.2018.05.057.

[44] Jaspreet Nagra. "Modelling Microstructure-Property Relationships in Polycrystalline Metals using New Fast Fourier Transform- Based Crystal Plasticity Frameworks". PhD thesis. Univeresity of Waterloo, Feb. 2019. DOI: 10.13140/RG.2.2.25091.45604.

[45] Ping Cheng et al. "Passively Q-switched Ytterbium-doped fiber laser based on broadband multilayer Platinum Ditelluride ($PtTe_2$) saturable absorber". In: *Scientific Reports* 9.1 (July 2019). ISSN: 2045-2322. DOI: 10.1038/s41598-019-46658-y.

[46] Edwin Owen and Eric Yates. "XLI. Precision measurements of crystal parameters". In: *London, Edinburgh, and Dublin Philosophical Magazine, and Journal of Science* (Feb. 1933), pp. 472–488. DOI: https://doi.org/10.1080/14786443309462199.

[47] Gloria Anemone et al. "Experimental determination of surface thermal expansion and electron–phonon coupling constant of 1T-$PtTe_2$". In: *2D Materials* 7.2 (Jan. 2020), p. 025007. ISSN: 2053-1583. DOI: 10.1088/2053-1583/ab6268.

[48] Ashish Badiye et al. "Introduction to Compound Microscope". In: *Taylor & Francis* (July 2022), pp. 72–82. DOI: 10.4324/9781003120995-5.

[49] Adel Racz and Miklós Menyhard. "Evaluation methods for XPS depth profiling; A review". In: *Applied Surface Science Advances* 30 (Dec. 2025), p. 100872. ISSN: 2666-5239. DOI: 10.1016/j.apsadv.2025.100872.

[50] John Moulder and Jill Chastain. *Handbook of X-ray Photoelectron Spectroscopy: A Reference Book of Standard Spectra for Identification and Interpretation of XPS Data*. Physical Electronics Division, Perkin-Elmer Corporation, 1992. ISBN: 978-0-9627026-2-4.

[51] Nobel Prize Foundation. *The Nobel Prize in Physics 1921*. 2025. URL: https://www.nobelprize.org/prizes/physics/1921/summary/.

[52] James Hillier. "Photo-engineered optoelectronic properties of transparent conductive oxides via reactive laser annealing (ReLA): the consequence of defects." PhD thesis. Eindhoven University of Technology, Sept. 2021. DOI: 10.13140/RG.2.2.15444.07047.

[53] Craig Klauber. "Refinement of magnesium and aluminium K_α X-ray source functions". In: *Surface and Interface Analysis* 20.8 (July 1993), pp. 703–715. ISSN: 0142-2421. DOI: 10.1002/sia.740200815.

[54] Curran Kalha et al. "Hard X-ray photoelectron spectroscopy: a snapshot of the state-of-the-art in 2020". In: *Journal of Physics: Condensed Matter* 33.23 (May 2021), p. 233001. ISSN: 0953-8984. DOI: 10.1088/1361-648X/abeacd.

[55] Joe Baio and Daniel Graham. "Surface analysis tools for characterizing biological materials". In: *Chemical Society Reviews* 49.11 (2020), pp. 3278–3296. DOI: 10.1039/D0CS00181C.

[56] Meng Li et al. "Research on AFM tip-related nanofabrication of two-dimensional materials". In: *Nanotechnology Reviews* 12.1 (Dec. 2023). ISSN: 2191-9097. DOI: 10.1515/ntrev-2023-0153.

[57] Muhammad K. Khan and Qingyuan Wang. *Atomic force microscopy (AFM) for materials characterization.* Woodhead Publishing, Jan. 2016, pp. 1–16. DOI: 10.1016/B978-0-08-100040-3.00001-8.

[58] Karolina Szafrańska. "Novel screening methods for nanoscale changes in liver cell fenestrations elicited by pharmaceuticals". PhD thesis. The Arctic University of Norway, Aug. 2022.

[59] Ewelina Lipiec et al. "Revealing DNA Structure at Liquid/Solid Interfaces by AFM-Based High-Resolution Imaging and Molecular Spectroscopy". In: *Molecules* 26.21 (Oct. 2021), p. 6476. ISSN: 1420-3049. DOI: 10.3390/molecules26216476.

[60] Sumaiya Shawkat et al. "Scalable Van der Waals Two-Dimensional PtTe2 Layers Integrated onto Silicon for Efficient Near-to-Mid Infrared Photodetection." In: *ACS applied materials & interfaces v13 n13 (20210407): 15542-15550* (2021). ISSN: 1944-8244. DOI: 10.1021/acsami.1c03512.

[61] Michel Hove and William Weinberg. *Low-Energy Electron Diffraction.* Springer, 1986. ISBN: 978-3-642-82721-1.

[62] Antonio Politano and Gennaro Chiarello. "Tailoring the surface chemical reactivity of transition-metal dichalcogenide $PtTe_2$ crystals". In: *Advanced Functional Materials* 28.15 (Apr. 2018), p. 1706504. ISSN: 1616-301X. DOI: 10.1002/adfm.201706504.

[63] Teterin Yuri and Konstantin Maslakov. "X-ray photoelectron study of charge states for bismuth and aluminum atoms in glasses luminescent in the infrared region". In: *Doklady Physics* 53.11 (Nov. 2008), pp. 566–570. ISSN: 1028-3358. DOI: 10.1134/S1028335808110049.

Acknowledgments

Although I am the author of this thesis, I could not have completed this research on my own, which is why I would like to thank the members of the Surfaces and Thin Films group that made this Master Research Project possible.

First of all, I would like to thank Antonija for giving me the opportunity to join her research group, for introducing me to this interesting research topic, and for her guidance and supervision throughout the project. Secondly, I would like to thank Douwe for always being ready to discuss the project with me, and thanks to his help the LEED, AFM, XPS, and optical microscopy results were gathered successfully. Finally, I would like to thank Dan and Dominic for providing support in the laboratory whenever it was needed.

Appendices

A Technical Drawings of Vacuum System Components

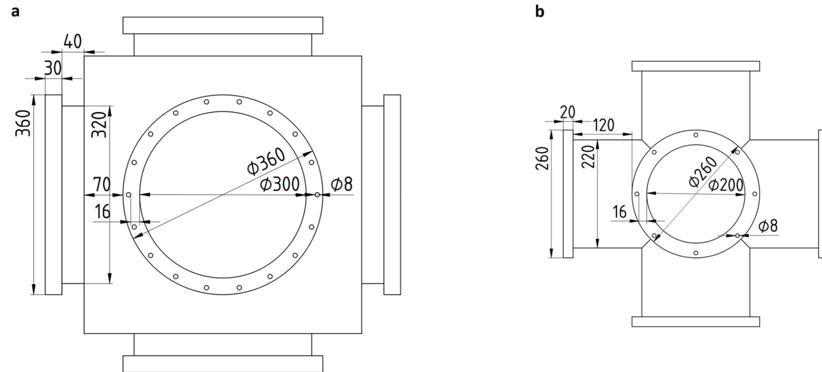

Figure 32: Technical drawing depicting the left, right, top, bottom, front, and back view of the a) preparation chamber, b) load lock chamber. Units of length are in millimeters.

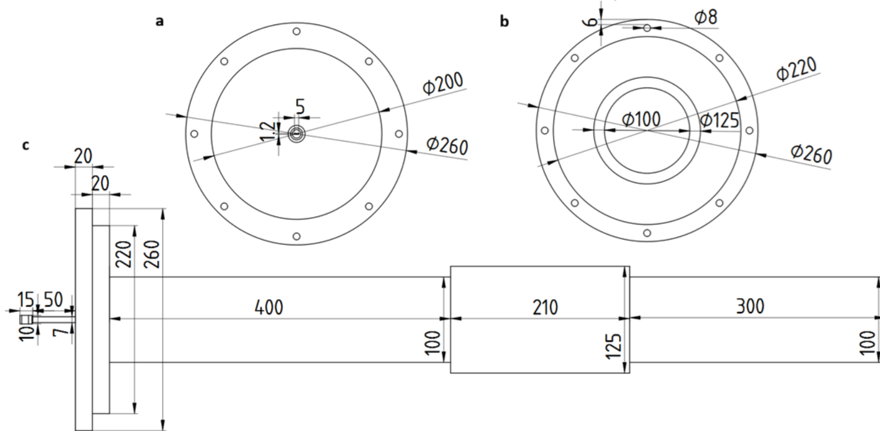

Figure 33: Technical drawing depicting the transfer arm viewed from the a) left, b) right, c) top, bottom, front, and back. Units of length are in millimeters.

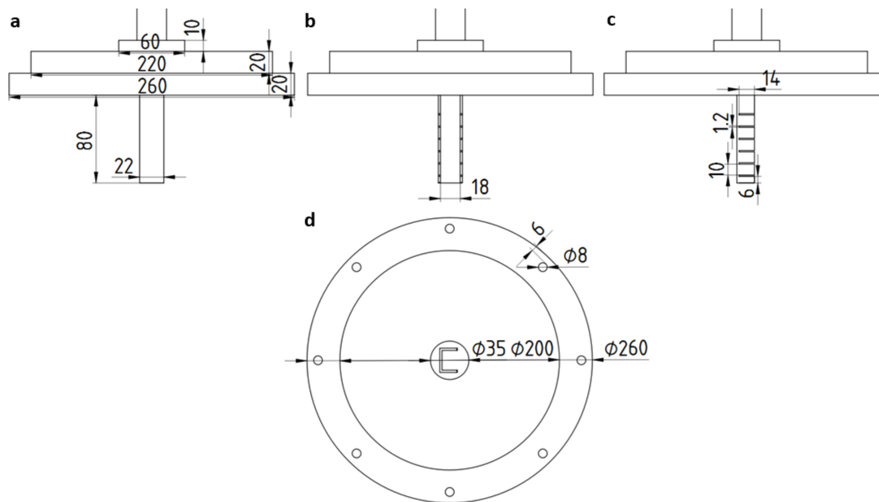

Figure 34: Technical drawing depicting the garage viewed from the a) left, b) right, c) back, d) bottom. Units of length are in millimeters.

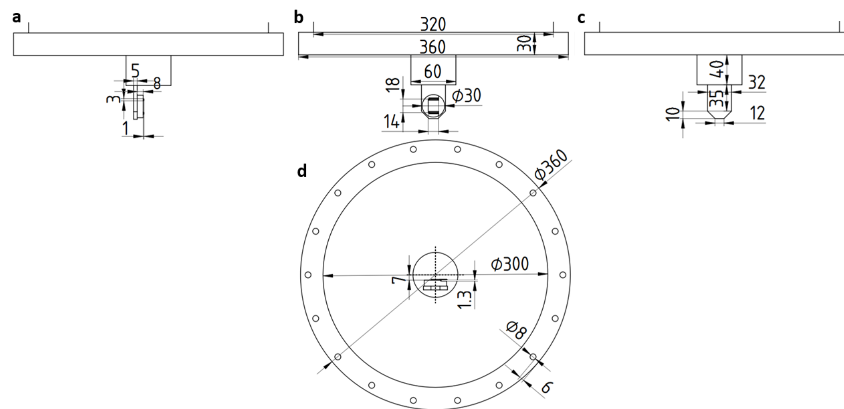

Figure 35: Technical drawing depicting the manipulator viewed from the a) left, b) front, c) left, and d) bottom. Units of length are in millimeters.

B Additional Optical Microscope Images

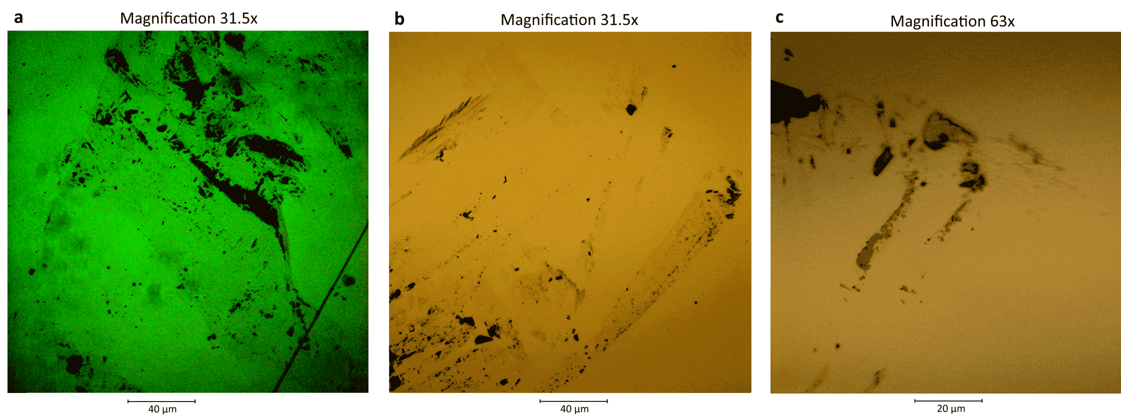

Figure 36: Optical microscope results without annotations, of Ag(111)/mica substrate with exfoliated a) $PtBi_2$, b) $Pt(BiTe)_2$, and $PtTe_2$.

C Supplementary High Resolution XPS Scans

The high resolution scans in the C 1s core-level domain of the exfoliation sites containing $PtBi_2$, $Pt(BiTe)_2$, and $PtTe_2$ are shown in Figures 37a, 37b, and 37c, respectively. The position of the C 1s peak was always used as a reference to calibrate the binding energy scale. Each fit includes a Shirley background indicated by a dashed line, and four symmetric Voigt peaks. The colored peaks indicate different different bonding environments of carbon. Green for hydrocarbons (C-C/C-H), purple for alcohol and ether groups (C-O), violet for carbonyl groups (C=O), and pink for carboxyl and ester groups (O-C=O).

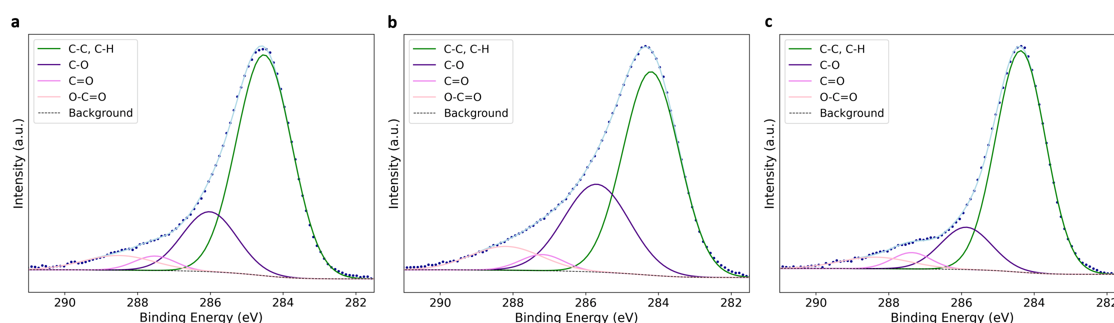

Figure 37: XPS narrow scan of the C 1s core-level, showing intensity as a function of binding energy of Ag(111)/mica with exfoliated a) $PtBi_2$, b) $Pt(BiTe)_2$, and c) $PtTe_2$.

High resolution scans in the O 1s core-level binding energy region of the exfoliation sites containing $PtBi_2$, $Pt(BiTe)_2$, and $PtTe_2$ are shown in Figures 38a, 38b, and 38c, respectively. Each fit includes a Shirley background represented by the dashed line. The symmetric green peak represents lattice oxygen bonded to tellurium (O-Te) and oxygen bonded to silver (O-Ag). The other peaks are symmetric, where purple corresponds to oxygen in carbon-containing surface species or contamination (O-C), and pink indicates adsorbed molecular water on the surface in the XPS spectrum. All samples contain similar amounts of O-Te and O-C. Only the $Pt(BiTe)_2$ and $PtTe_2$ samples were measured to contain adsorbed water, even though all three samples were transferred and exposed to an ambient environment

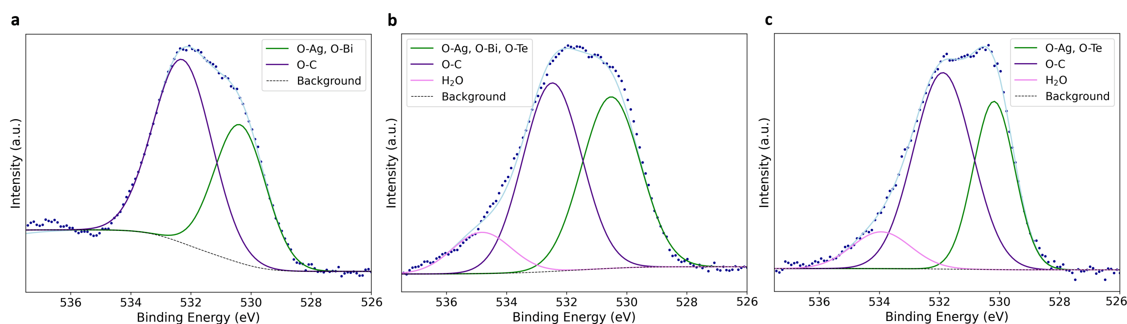

Figure 38: XPS narrow scan of the O 1s core-level, showing intensity as a function of binding energy of Ag(111)/mica with exfoliated a) $PtBi_2$, b) $Pt(BiTe)_2$, and c) $PtTe_2$.

Furthermore, high-resolution scans of the Ag 3d core-level region for the $PtBi_2$, $Pt(BiTe)_2$, and $PtTe_2$ exfoliation sites are presented in Figures 39a, 39b, and 39c, respectively. Each fit includes a Shirley background represented by the dashed line. Fur-

thermore, the light blue asymmetric peaks correspond to metallic silver (Ag(0)), while the green symmetric peaks represent oxidized silver (Ag-O). The metallic silver peaks are visible in all samples, while the oxidized silver peak is only well pronounced in the sample containing $Pt(BiTe)_2$.

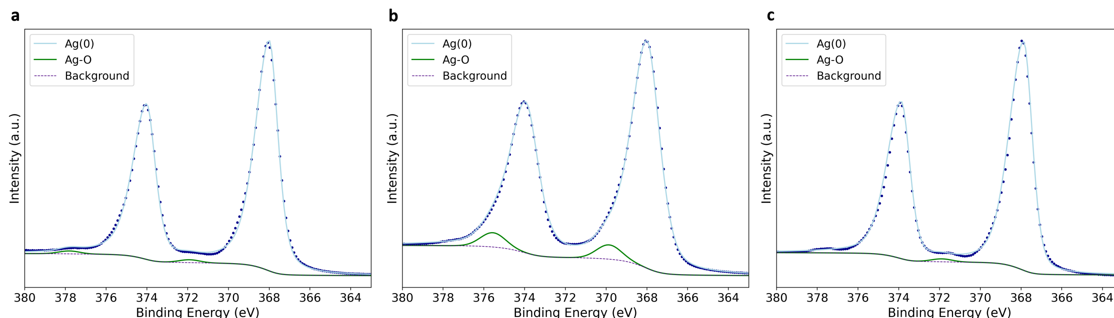

Figure 39: XPS narrow scan of the Ag 3d core-level, showing intensity as a function of binding energy of Ag(111)/mica with exfoliated a) $PtBi_2$, b) $Pt(BiTe)_2$, and c) $PtTe_2$.

D Atomic Percentages of Chemical Environments

Element	Chemical Environment	Normalized Area (Counts·eV)	Atomic Percentage (%)
C 1s	C-C/C-H	52183.5	19.22
	C-O	13984	5.15
	C=O	2535.66	0.93
	O-C=O	4432.11	1.63
O 1s	O-O/O-C	15950.41	5.87
	O-Bi	24102.03	8.87
Pt 4f	Pt(0)	2919.01	1.07
Bi 4f	Bi(0)	7548.96	2.78
	Bi-O	10850.56	4.00
	Bi=O	5190.86	1.91
S 2p	S 2p	39681.11	14.61
Ag 2d	Ag(0)	91189.75	33.58
	Ag-O	1005.78	0.37

Table 4: Chemical environment atomic percentages, derived from normalized peak areas in the XPS narrow-scan spectra of the $PtBi_2$ exfoliation site on Ag(111)/mica.

Element	Chemical Environment	Normalized Area (Counts·eV)	Atomic Percentage (%)
C 1s	C-C/C-H	80486	18.41
	C-O	40148	9.19
	C=O	4938	1.13
	O-C=O	11836	2.71
O 1s	O-O/O-C	34294.31	7.85
	O-Bi	37732.11	8.63
	H_2O	8243.90	1.89
Pt 4f	Pt(0)	1747.26	0.40
Bi 4f	Bi(0)	62.99	0.01
	Bi-O	2286.98	0.52
	Bi=O	3461.72	0.79
S	S 2p	54138.33	12.39
Te	Te-Pt	671.37	0.15
	Te-O	766.81	0.18
Ag 2d	Ag(0)	148246.90	33.92
	Ag-O	8021.16	1.84

Table 5: Chemical environment atomic percentages, derived from normalized peak areas in the XPS narrow-scan spectra of the Pt(BiTe)$_2$ exfoliation site on Ag(111)/mica.

Element	Chemical Environment	Normalized Area (Counts·eV)	Atomic Percentage (%)
C 1s	C-C/C-H	30432	23.91
	C-O	5943	4.67
	C=O	1739	1.37
	O-C=O	2257	1.77
O 1s	O-O/O-C	8900.41	6.99
	O-Bi	14779.67	11.61
	H_2O	2765.85	2.17
Pt 4f	Pt(0)	2919.01	2.29
Te	Te-Pt	5.12	0.004
	Te-O	15.12	0.012
Ag 2d	Ag(0)	56854.63	44.67
	Ag-O	661.05	0.52

Table 6: Chemical environment atomic percentages, derived from normalized peak areas in the XPS narrow-scan spectra of the PtTe$_2$ exfoliation site on Ag(111)/mica.